Tumor-Derived CCL16 Normalizes Tumor Vasculature through Macrophage ICAM-1 Receptor and Enhances Immunotherapy Efficacy in Hepatocellular Carcinoma

Kunling Chen[1], Huolun Feng[2], Yujie Zhang[3], Jingyuan Pei[1], Yuyan Xu[1], Xiangxu Wei[1], Zhuohao Chen[1], Zhoubin Feng[1], Lei Cai[1], Yong Li[2], Liang Zhao[3], and Mingxin Pan[1]

ABSTRACT

Hepatocellular carcinoma (HCC) is characterized by aberrant tumor vasculature and an immunosuppressive tumor microenvironment (TME), both of which compromise immunotherapy efficacy while promoting circulating tumor cell (CTC) dissemination and immune escape. In this study, we aimed to identify potential therapeutic targets for remodeling aberrant tumor vasculature by analyzing CTCs from patients with early-stage HCC. HCC tissue samples derived from patients with elevated CTC counts demonstrated significant *CCL16* downregulation accompanied by vascular structural abnormalities and an immunosuppressive TME. *CCL16* deficiency in murine models exacerbated both vascular dysfunction and immunosuppressive TME formation, whereas *CCL16* overexpression mediated vascular normalization and promoted immune cell infiltration. Mechanistically, *CCL16* interacted with *ICAM-1* receptor on tumor-associated macrophages, triggering *JAK2–STAT6* pathway activation and subsequent *IL24* secretion. Pharmacologic intervention using sitagliptin, a DPP4 inhibitor, effectively stabilized tumor vasculature by preventing *CCL16* degradation. Importantly, therapeutically elevating *CCL16* levels combined with anti–PD-1 antibody administration synergistically enhanced vascular normalization and improved antitumor immunity in HCC models, suppressing tumor growth. These findings establish *CCL16* as a critical regulator of vascular–immune crosstalk and propose DPP4 inhibition as a promising therapeutic strategy for treating HCC.

Significance: *CCL16* regulates *IL24* secretion by macrophages to promote vascular normalization and immune infiltration in hepatocellular carcinoma, which can be harnessed using DPP4 inhibition to enhance the efficacy of immunotherapy.

Introduction

Hepatocellular carcinoma (HCC) is a highly vascularized and immune-evasive solid tumor (1, 2). Antiangiogenic drugs are fundamental components in advanced HCC treatment, inhibiting excessive tumor vascular growth (3) and demonstrating potential for inducing vascular normalization (4, 5). Although antiangiogenic agents like lenvatinib can partially reshape abnormal tumor vasculature (6), their optimal dosage and therapeutic window are narrow and challenging to determine (7). Moreover, the indiscriminate application of antiangiogenic agents can lead to excessive pruning of tumor vasculature and in severe cases, complete vascular loss and tumor progression (8, 9). Additionally, these drugs may induce cellular reprogramming of tumor cells, immune cells, and local stromal components within the tumor microenvironment (TME), resulting in drug resistance and therapeutic failure (10, 11). Consequently, there is an urgent need to identify more suitable drugs or molecular targets for reshaping HCC vasculature.

Tumor vascular normalization (TVN) is a promising strategy for enhancing cancer therapy efficacy by improving drug delivery and modulating the TME (12, 13). Abnormal and dysfunctional tumor vasculature often exhibits poor characteristics, such as irregular morphology, excessive permeability, and inadequate perfusion (8). Notably, abnormal tumor vasculature promotes immune evasion, tumor progression, and metastasis (9). The concept of TVN aims to restore the balance between proangiogenic and antiangiogenic factors, improve vascular function, reduce hypoxia, and increase drug penetration (4). This approach also enhances immune cell infiltration, thereby creating a more favorable TME for antitumor immunity (14).

Accumulating evidence suggests that tumor vasculature is primarily regulated by tumor-associated macrophages (TAM; ref. 15). Reprogramming TAMs, particularly hypoxia-associated TAMs, can remodel tumor vasculature and facilitate the infiltration of cytotoxic immune cells in the TME (16). Similarly, targeting the polarization

---

[1]General Surgery Center, Department of Hepatobiliary Surgery II, Guangdong Provincial Research Center for Artificial Organ and Tissue Engineering, Guangzhou Clinical Research and Transformation Center for Artificial Liver, Institute of Regenerative Medicine, Zhujiang Hospital, Southern Medical University, Guangzhou, China. [2]Department of Gastrointestinal Surgery, Department of General Surgery, Guangdong Provincial People's Hospital (Guangdong Academy of Medical Sciences), Southern Medical University, Guangzhou, China. [3]Department of Pathology & Guangdong Province Key Laboratory of Molecular Tumor Pathology, School of Basic Medical Sciences, Southern Medical University, Guangzhou, China.

K. Chen, H. Feng, Y. Zhang, and J. Pei contributed equally to this article.

Corresponding Authors: Mingxin Pan, General Surgery Center, Department of Hepatobiliary Surgery II, Guangdong Provincial Research Center for Artificial Organ and Tissue Engineering, Guangzhou Clinical Research and Transformation Center for Artificial Liver, Institute of Regenerative Medicine, Zhujiang Hospital, Southern Medical University, Guangzhou 510000, China. E-mail: panmx@smu.edu.cn; Lei Cai, cail_427@smu.edu.cn; Liang Zhao, Department of Pathology & Guangdong Province Key Laboratory of Molecular Tumor Pathology, School of Basic Medical Sciences, Southern Medical University, Guangzhou 510000, China. E-mail: zhaol828@smu.edu.cn; and Yong Li, Department of Gastrointestinal Surgery, Department of General Surgery, Guangdong Provincial People's Hospital (Guangdong Academy of Medical Sciences), Southern Medical University, Guangzhou 510080, China. E-mail: liyong@gdph.org.cn

Cancer Res 2025;85:3633–50

doi: 10.1158/0008-5472.CAN-24-4323

states of TAMs represents a promising therapeutic strategy to modulate tumor vasculature and enhance antitumor immune responses (17). Targeting angiogenic TAM subsets has been shown to improve tumor vascular function (18). Downregulating the expression of proangiogenic factors in TAMs suppresses angiogenesis, thereby promoting the normalization of tumor blood vessels.

The efficacy of immunotherapy and antiangiogenic therapy in advanced HCC remains suboptimal, primarily because of irreversibly aberrant tumor vasculature and an immunosuppressive TME (19). The hyperpermeable abnormal vascular network facilitates circulating tumor cell (CTC) dissemination (20), whereas the immunosuppressive TME promotes CTC immune evasion (21, 22) and subsequent metastatic spread. Consequently, early intervention to restore TVN and alleviate the immunosuppressive TME is critical. Through CTC detection via liquid biopsy (23), we aimed to identify potential therapeutic targets for remodeling aberrant tumor vasculature by analyzing key genes in CTCs from patients with early-stage HCC.

In this study, we demonstrate that CCL16 can remodel abnormal tumor vasculature, enhancing immunotherapy efficacy and suppressing tumor progression. We further elucidate that CCL16-induced TVN is mediated by macrophages with the ICAM-1 receptor. Mechanistically, CCL16 interacts with ICAM-1 on TAMs, activating the JAK2–STAT6 pathway and promoting IL24 secretion, which in turn normalizes tumor vasculature. Additionally, based on the proteolytic activity of DPP4, we show that sitagliptin, a clinically used DPP4 inhibitor (DPP4i) for diabetes treatment, prevents CCL16 degradation, further enhancing TVN. Hence, we propose that CCL16 may serve as a valuable tool for TVN in the treatment of patients with HCC, particularly in the context of immunotherapies.

Materials and Methods

Patients and clinical specimens

Tumor tissues from patients with HCC and paired paracancerous tissues were obtained from the Department of Hepatobiliary Surgery II, Zhujiang Hospital, Southern Medical University. Serum samples were obtained from healthy volunteers and patients with HCC. Written informed consent was obtained from all participants or their legal guardians prior to sample collection. The Zhujiang Hospital Ethics Committee of Southern Medical University approved this study (ethics code: 2023-KY-199-01), and all aspects of the study complied with the Declaration of Helsinki.

Mice

C57BL/6 mice (RRID: IMSR_JAX:000664) and nude mice were purchased from the Guangdong Medical Laboratory Animal Center and the Southern Medical University Experimental Animal Center. All studies were performed in male mice unless otherwise indicated. Mice were kept in a standard 12-hour light–dark cycle under the specific pathogen-free conditions and were allowed free access to water and food. All the mice we used were healthy and immune normal. Animal-related research protocols are consistent with the U.S. Public Health Service Policy on Use of Laboratory Animals and were approved by the Ethics Committee on Use and Care of Animals of Zhujiang Hospital, Southern Medical University (ethics code: LAEC-2023-141).

Cell lines and cell culture

All cells were incubated at 37°C in a humidified atmosphere containing 5% CO_2. Huh7 cells (RRID: CVCL_0336), Hepa1-6 cells (RRID: CVCL_0327), THP-1 cells (RRID: CVCL_0006), and human umbilical vein endothelial cells (RRID: CVCL_2959) were obtained from iCell with short tandem repeat certifications. Huh7 and Hepa1-6 were cultured in DMEM (GE Healthcare, SH30243.FS) supplemented with 10% FBS (Gibco) and 1% penicillin–streptomycin (Gibco). THP-1 cells and human umbilical vein endothelial cells were maintained in RPMI-1640 medium (Gibco) with 10% FBS and 1% penicillin–streptomycin and used for *in vitro* experiments within five passages. Culture medium was refreshed every 2 to 3 days to maintain cells in the logarithmic growth phase. CCL16-overexpressing and short hairpin RNA–mediated knockdown lentiviral plasmids were constructed and packaged using a lentiviral expression system (GeneChem). Huh7 and Hepa1-6 cells were infected with the lentiviruses, and stable cell lines were selected using puromycin (2 μg/mL). All cells were routinely tested for *Mycoplasma* contamination using the GMyc-PCR Mycoplasma Test Kit (Yeasen, cat. #40601ES20).

Detection and quantification of CTCs

CTCs were detected using liquid biopsy technology. Peripheral blood samples (10 mL) were collected from patients in EDTA tubes. The samples were centrifuged at 1,500 *g* for 10 minutes at 4°C, and the supernatant was discarded, retaining the pellet for further analysis. The CanPatrol CTC analysis system (Surexam) was used to detect the number of CTCs (24). Blood samples were processed with the CellSearch kit, in which CTCs were enriched by immunomagnetic separation using anti-EpCAM antibodies. The enriched cells were stained with immunofluorescent antibodies against cytokeratins (CK8, CK18, and CK19) and CD45 to exclude leukocytes. The number of CTCs per mL of blood was quantified using an automated microscope in the CellSearch system. Based on CTC counts, samples were categorized into two groups: CTC low (fewer than three CTCs) and CTC high (more than or equal to three CTCs).

RNA sequencing of HCC tissues

Total RNA was extracted from four HCC tissues per group (CTC low and CTC high) using TRIzol reagent (30 mg tissue/sample). RNA integrity was verified via Agilent 2100 Bioanalyzer. Libraries were prepared from high-quality RNA and sequenced on an Illumina NovaSeq 6000 platform. Raw reads were quality controlled using FastQC, aligned to the human reference genome via HISAT2 (RRID: SCR_015530), and quantified using StringTie. Differential expression analysis was performed with DESeq (RRID: SCR_000154). Visualization of differentially expressed genes (DEG) included volcano plots and heatmaps. Functional enrichment analysis of DEGs was conducted using clusterProfiler (RRID: SCR_016884).

Western blotting

Whole-cell lysates were prepared using cell lysis buffer (Beyotime Biotechnology) and boiled in SDS sample loading buffer. For conditioned culture medium analysis, equal numbers of cells were seeded, and 4 mL of supernatant was collected and concentrated using ultrafiltration tubes centrifuged at 4,000 × g for 15 minutes. The concentrated protein was denatured, and equal volumes were loaded for analysis. Equal amounts of protein (30 μg per lane) were separated by 10% SDS-PAGE and transferred to polyvinylidene difluoride membranes (Millipore). The membranes were blocked with 5% nonfat milk in Tris-Buffered Saline with Tween 20 (TBST) for 1 hour at room temperature, followed by overnight incubation at 4°C with the following primary antibodies: anti–β-tubulin (TA-10, ZsBio), anti–β-actin (TA-09, ZsBio), anti-CCL16 (YN1319, Immunoway), anti–ICAM-1 (10831-1-AP, Proteintech), anti-JAK2 (ET1607-35,

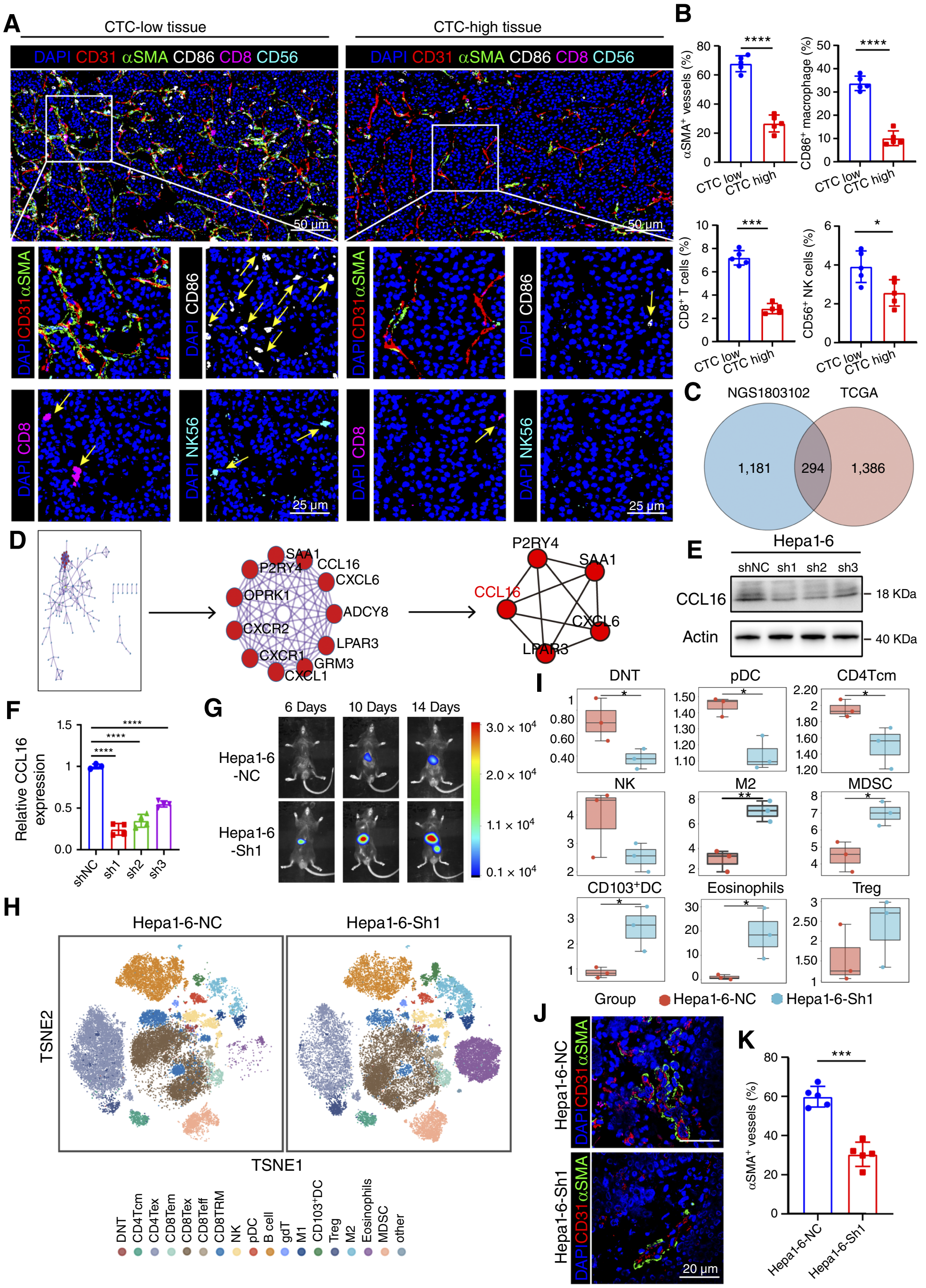

Figure 1.

CCL16 emerges as a potential crucial regulatory molecule in the vascular and immune microenvironment of HCC. **A** and **B,** Representative multiplex IHC images (**A**) and quantification (**B**) of αSMA$^+$ vessels and infiltrating immune cells including CD8$^+$ T cells, CD86$^+$ macrophages, and CD56$^+$NK cells in CTC-low tissue and CTC-high tissue ($n = 5$). Scale bars, 50 and 25 μm. **C,** 294 intersecting genes between the NGS1803102 (high-throughput sequencing of tissue samples related to CTCs) and TCGA-LIHC dataset. **D,** Five key genes in the core module through protein–protein interaction network analysis and the cytoHubba tool. **E** and **F,** Protein (**E**) and mRNA levels (**F**) of CCL16 in Hepa1-6 cells transduced with lentiviral short hairpin RNA targeting CCL16 (Hepa1-6-Sh) or nontargeting control short hairpin RNA (Hepa1-6-NC). **G,** Representative luciferase-based bioluminescence images of C57BL/6 mice injected orthotopically into the liver, with indicated cells on day 6, day 10, and day 14 ($n = 5$ mice per group). **H,** Mass cytometry profiles reflecting infiltration of immune cell subsets in indicated tumors. **I,** Quantification of different immune cell subsets in indicated tumors. **J** and **K,** Representative IF images (**J**) and quantification (**K**) of αSMA$^+$ pericyte coverage of CD31$^+$ tumor vessels in indicated tumors ($n = 5$). Scale bars, 20 μm. Statistical significance assessed using a two-tailed unpaired Student *t* test (**B** and **K**) or a one-way ANOVA (**F**). Representative of $n = 3$ independent experiments (**E**). *, $P < 0.05$; ***, $P < 0.001$; ****, $P < 0.0001$. DC, dendritic cell; MDSC, myeloid-derived suppressor cell; Treg, regulatory T cell; TSNE, t-distributed stochastic neighbor embedding.

HUABIO), anti–pJAK2 (ET1607-34, HUABIO), anti-STAT6 (51073-1-AP, Proteintech), anti–pSTAT6 (ab188080, Abcam), anti-DPP4 (DF12387, Affinity), anti-IL24 (26772-1-AP, Proteintech), anti-F4/80 (28463-1-AP, Proteintech), anti-CCR1 (DF2710, Affinity), anti-CD31 (ab124432, Abcam), anti-SMA (ZM-0003, ZsBio), anti-GST (#2625, Cell Signaling Technology), and anti-FLAG (F1804, Sigma-Aldrich). After washing with TBST, the membranes were incubated with fluorescein-conjugated secondary antibodies for 1 hour at room temperature. The immunoblots were visualized using the ultrahigh-sensitivity chemiluminescence imaging system ChemiDoc XRS+ (Bio-Rad Laboratories) and relative protein levels were quantified using ImageJ software (NIH). A full list of antibodies and detailed information are provided in Supplementary Table S1.

qRT-PCR

Total RNA was isolated using TRIzol reagent (Takara) according to the manufacturer's instructions. For each sample, 1 μg of purified RNA was reverse transcribed into cDNA using

PrimeScript RT Master Mix (Takara). qRT-PCR was performed on a LightCycler 480 System (Roche) with SYBR Green PCR Master Mix (Takara). The cycling conditions were initial denaturation at 95°C for 30 seconds, followed by 40 cycles of 95°C for 5 seconds and 60°C for 30 seconds. Relative gene expression levels were calculated using the $2^{-\Delta\Delta CT}$ method and normalized to GAPDH.

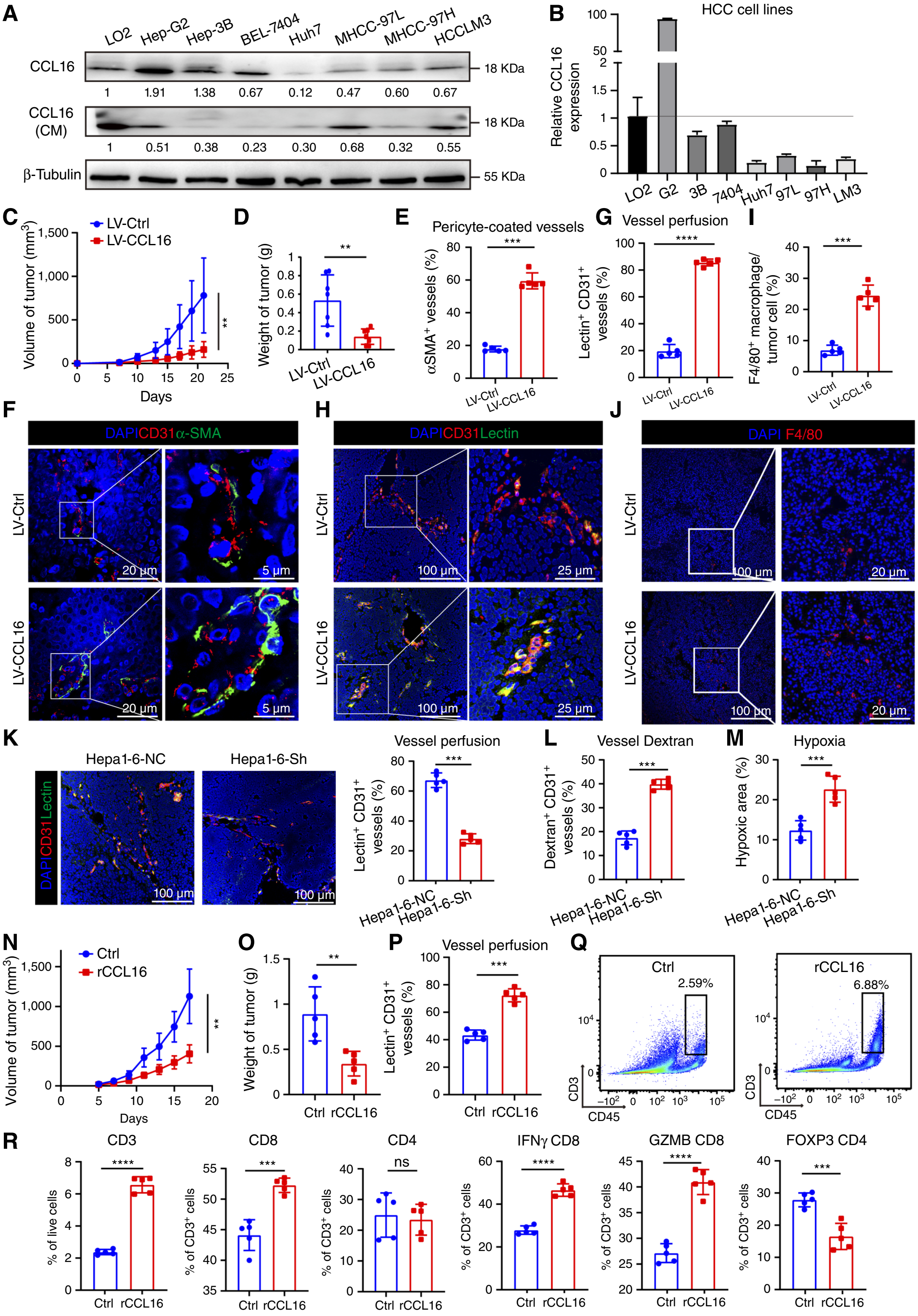

Primer sequences used for qPCR are provided in Supplementary Table S2.

Mass cytometry

Tumor tissues were collected and digested with trypsin to prepare single-cell suspensions. Cells were isolated by Ficoll-Paque density gradient centrifugation and resuspended in RPMI-1640 medium supplemented with 10% FBS. A total of 1×10^6 cells were incubated with 1 μmol/L cisplatin for 5 minutes to distinguish dead cells. Cells were then stained with metal-conjugated antibodies against surface markers, including anti-CD45, anti-CD3e, anti-CD4, anti-CD8, anti-NK1.1, anti-CD11b, anti-F4/80, anti–Gr-1, and 42 other markers, for 30 minutes. After fixation and permeabilization, the cells were stained with antibodies targeting intracellular markers for 45 minutes. Samples were barcoded using the Cell-ID 20-Plex Pd Barcoding Kit and pooled. The technical guidance and experimental instruments were provided by Protin Health Technology Co., Ltd. Data were acquired using the Helios mass cytometer and normalized using CyTOF software. Data were debarcoded, and cell subsets were analyzed using t-SNE and FlowSOM. Statistical differences between groups were assessed using unpaired Student *t* tests or Mann–Whitney U tests in R 4.0.0 or GraphPad Prism 9.0.

Flow cytometric analysis

Tumor tissues were minced and digested with collagenase IV (40510ES76, Yeasen) and DNase I (1121MG010, Biofroxx) for 30 minutes at 37°C. Single-cell suspensions were filtered through a 70-μm strainer and incubated with Fc block. Cells were first stained with Zombie Red Fixable Viability Dye (423109, BioLegend) to exclude dead cells. For surface staining, the cells were incubated with the following fluorochrome-conjugated antibodies for 30 minutes at 4°C: human CD45-Alexa Fluor 647 (304018, BioLegend), human CD3-PerCP/Cy5.5 (317336, BioLegend), human CD8-APC (344721, BioLegend), Brilliant Violet 510 anti–mouse CD45 (103138, BioLegend), PE/Cy7 anti–mouse CD4 (100528, BioLegend), APC/Cy7 anti–mouse CD3ε (100330, BioLegend), Alexa Fluor 700 anti–mouse CD8a (100730, BioLegend), PerCP/Cy5.5 anti–mouse/human CD11b (101228, BioLegend), Brilliant Violet 785 anti–mouse F4/80 (123141, BioLegend), FITC anti–mouse NK-1.1 (108706, BioLegend), PE anti–mouse Ly-6G/Ly-6C (108407, BioLegend), FITC rat anti–mouse CD45 (553079, BD Pharmingen), and MS CD4 BV650 GK1.5 (563232, BD Pharmingen). For intracellular staining, the cells were fixed and permeabilized using a Cytofix/Cytoperm kit (BD Biosciences), followed by staining with Alexa Fluor 647 anti–mouse/rat/human FOXP3 (320014, BioLegend), Brilliant Violet 605 anti–mouse IFNγ (505840, BioLegend), Brilliant Violet 421 anti–mouse lFNγ (505829, BioLegend), anti–mouse granzyme B PE-Cy7 (25-8898-80, Thermo Fisher Scientific), and PE rat anti–mouse Foxp3 (R16-715; 563101, BD Pharmingen). Data acquisition was performed using a BD LSRFortessa flow cytometer and analyzed with FlowJo software (RRID: SCR_008520). A full list of antibodies and detailed information are provided in Supplementary Table S3.

IHC staining

IHC staining was performed on formalin-fixed, paraffin-embedded tissue sections from human HCC and mouse tumor xenografts. Tissue sections were deparaffinized, rehydrated, and subjected to antigen retrieval using citrate buffer (pH 6.0) at 95°C for 20 minutes. Endogenous peroxidase activity was blocked with 3% hydrogen peroxide for 10 minutes. Sections were incubated with primary antibodies targeting specific proteins, followed by secondary antibody incubation and visualization using 3,3-diaminobenzidine as the chromogen. Sections were counterstained with hematoxylin, dehydrated, and mounted for microscopic analysis.

Multiplex IHC staining

Multiplex immunohistochemistry was performed using sequential staining to evaluate coexpression of five markers (CD31, αSMA, CD8, CD86, and CD56) on formalin-fixed, paraffin-embedded tissue sections. Briefly, sections were deparaffinized, rehydrated, and subjected to antigen retrieval. After blocking endogenous peroxidase and nonspecific binding, slides were incubated with the primary antibody against CD31 (1:200), followed by a horseradish peroxidase (HRP)–conjugated secondary antibody. Color development was achieved using 3-amino-9-ethylcarbazole chromogen, followed by hematoxylin counterstaining, dehydration, and mounting. For subsequent markers (αSMA, CD56, CD8, and CD86), the staining protocol was repeated sequentially after stripping prior antibodies via ethanol-based elution. High-resolution whole-slide imaging was performed using a fluorescence microscope. Pericyte coverage was quantified by calculating the percentage of $CD31^+$ vessels colocalized with $αSMA^+$ pericytes using ImageJ software (RRID: SCR_003070). Image analysis thresholds were calibrated against negative controls to ensure specificity.

Tumor vascular perfusion assay

Mice were injected intravenously with 40 mg/kg dextran or 10 mg/kg FITC-lectin (Sigma-Aldrich) dissolved in PBS (200 μL). After 10 minutes, mice were euthanized and perfused with 4% paraformaldehyde via the left ventricle after thoracotomy. Tumors were excised and fixed in sequential immersion in 20% and 30% PBS-buffered sucrose until they sank. Tumors were embedded in optimal cutting temperature and sectioned at 5 μm thickness.

Figure 2.

CCL16 promotes vascular normalization and reverses immunosuppressive TME in HCC. **A,** Protein levels and secreted protein in conditioned medium (CM) of CCL16 in human normal liver cell and liver cancer cells. **B,** mRNA levels of CCL16 in human normal liver cell and liver cancer cells. **C** and **D,** Tumor growth curves (**C**) and tumor weight (**D**) in nude mice injected subcutaneously with indicated cells for 21 days ($n = 7$ mice per group). **E** and **F,** Quantification (**E**) and representative IF images (**F**) of pericyte ($αSMA^+$) coverage of tumor vessels ($CD31^+$) in indicated tumors ($n = 5$). Scale bars, 20 and 5 μm. **G** and **H,** Quantification (**G**) and representative IF images (**H**) of vascular perfusion in indicated tumors using lectin fluorescence ($n = 5$). Scale bars, 100 and 25 μm. **I** and **J,** Quantification (**I**) and representative IF images (**J**) of $F4/80^+$ macrophages in indicated tumors ($n = 5$). Scale bars, 200 and 50 μm. **K,** Representative IF images and quantification of vascular perfusion in indicated tumors using lectin fluorescence ($n = 5$). Scale bars, 100 μm. **L,** Quantification of vascular leakage in indicated tumors using dextran fluorescence ($n = 5$). Scale bars, 100 and 20 μm. **M,** Quantification of tissue hypoxia in indicated tumors using hypoxyprobe ($n = 5$). Scale bars, 200 and 50 μm. **N** and **O,** Tumor growth curves (**N**) and tumor weight (**O**) in C57BL/6 mice injected subcutaneously with indicated cells ($n = 5$ mice per group). **P,** Quantification of vascular perfusion in indicated tumors using lectin fluorescence ($n = 5$). Scale bars, 100 μm. **Q,** Flow cytometry image of T cells in indicated tumors. **R,** Proportion of T cells, $CD8^+$ T cells, $CD4^+$ T cells, $IFNγ^+CD8^+$ T cells, $GZMB^+CD8^+$ T cells, and $FOXP3^+CD4^+$ T cells in indicated tumors. Statistical significance assessed using a two-way ANOVA test (**C** and **N**) or a two-tailed Student *t* test (**D, E, G, I, K–M, O, P,** and **R**). Representative of $n = 3$ independent experiments (**A** and **B**). ns, not significant; **, $P < 0.01$; ***, $P < 0.001$; ****, $P < 0.0001$. Ctrl, control; GZMB, granzyme B.

Sections were counterstained with DAPI and analyzed using confocal microscopy (FLUOVIEW FV3000, Olympus).

Immunofluorescence

Excised tumor tissues were embedded in paraffin or frozen in optimal cutting temperature. Endothelial cells were stained with anti-CD31 antibodies (ab124432, Abcam) and pericytes with anti–αSMA antibodies (ZM-0003, ZsBio). Hypoxia markers (pimonidazole), vascular leakage markers (dextran), and perfusion markers (lectin) were stained using fluorescently labeled secondary antibodies. Nuclei were counterstained with DAPI. Images were captured and analyzed with a confocal microscope (FLUOVIEW FV3000, Olympus). Vascular density and pericyte coverage were quantified in five random fields of view using ImageJ.

Gel electrophoresis and mass spectrometry analysis

THP-1 cells were differentiated into M0 macrophages by treatment with 100 nmol/L phorbol 12-myristate 13-acetate (PMA) for

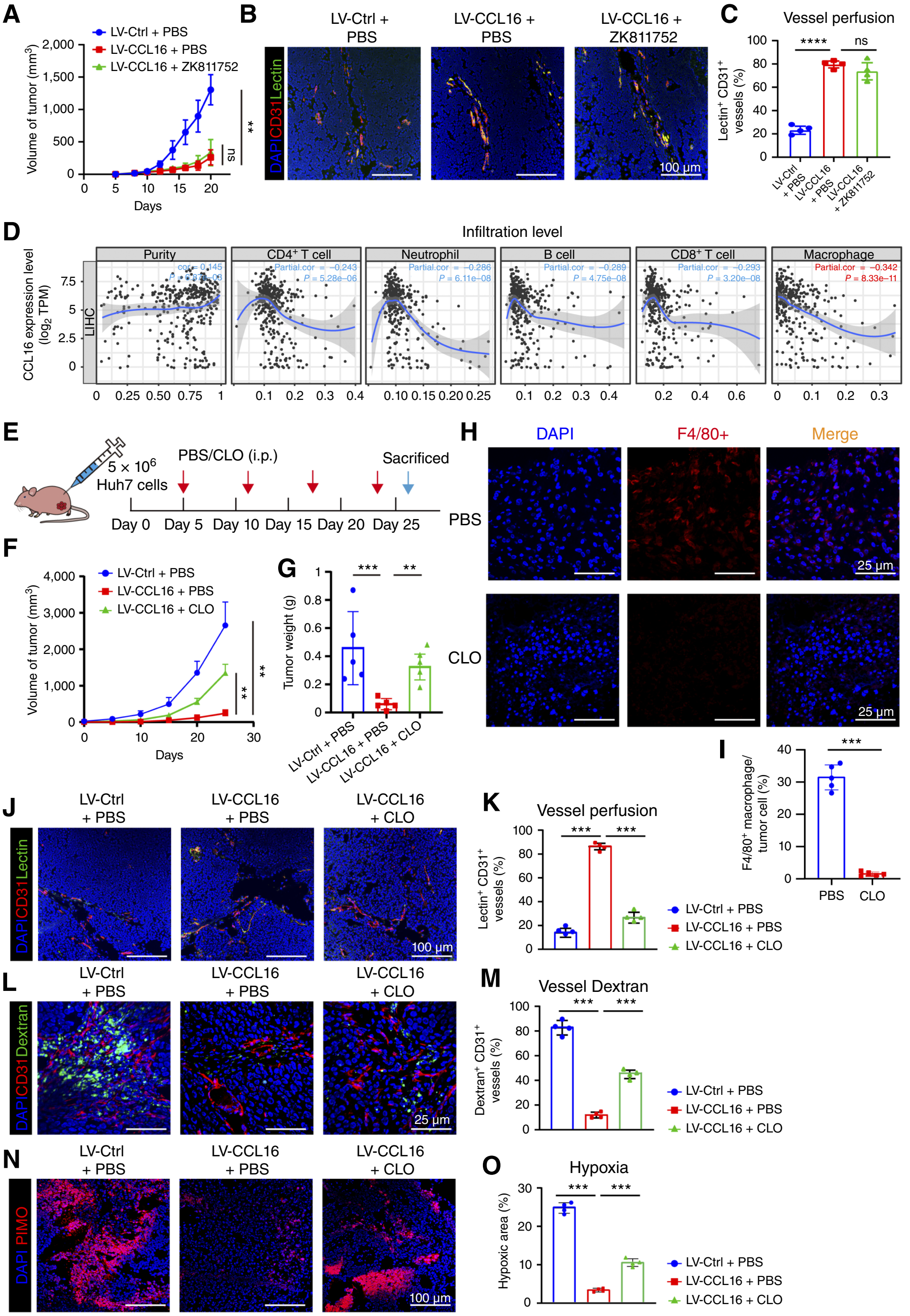

Figure 3.

CCL16 regulates macrophage-mediated TVN. **A,** Tumor growth curves in nude mice injected subcutaneously with indicated cells with or without the treatment of ZK811752. **B** and **C,** Representative IF images (**B**) and quantification (**C**) of pericyte (αSMA^+) coverage of tumor vessels ($CD31^+$) in indicated tumors ($n = 4$). Scale bars, 100 μm. **D,** Correlation between CCL16 expression and different immune cells in HCC from the TIMER database. **E–G,** Scheme representing the experimental procedure (**E**), tumor growth curves (**F**), and tumor weight (**G**) of nude mice injected subcutaneously with indicated cells with the treatment of PBS or clodronate liposome (200 μL per mouse). **H** and **I,** Representative IF images (**H**) and quantification (**I**) of $F4/80^+$ macrophages with the treatment of PBS or clodronate liposome in LV-CCL16 tumor ($n = 5$). Scale bars, 25 μm. **J** and **K,** Representative IF images (**J**) and quantification (**K**) of vascular perfusion in indicated tumors using lectin fluorescence ($n = 5$). Scale bars, 100 μm. **L** and **M,** Representative IF images (**L**) and quantification (**M**) of vascular leakage in indicated tumors using dextran fluorescence ($n = 5$). Scale bars, 25 μm. **N** and **O,** Representative IF images (**N**) and quantification (**O**) of tissue hypoxia in indicated tumors using hypoxyprobe ($n = 5$). Scale bars, 100 μm. Statistical significance assessed using a two-way ANOVA (**A** and **E**), one-way ANOVA (**B, F,** and **L–N**), and two-tailed unpaired Student *t* test (**K**). ns, not significant; **, $P < 0.01$; ***, $P < 0.001$; ****, $P < 0.0001$. CLO, clodronate liposome.

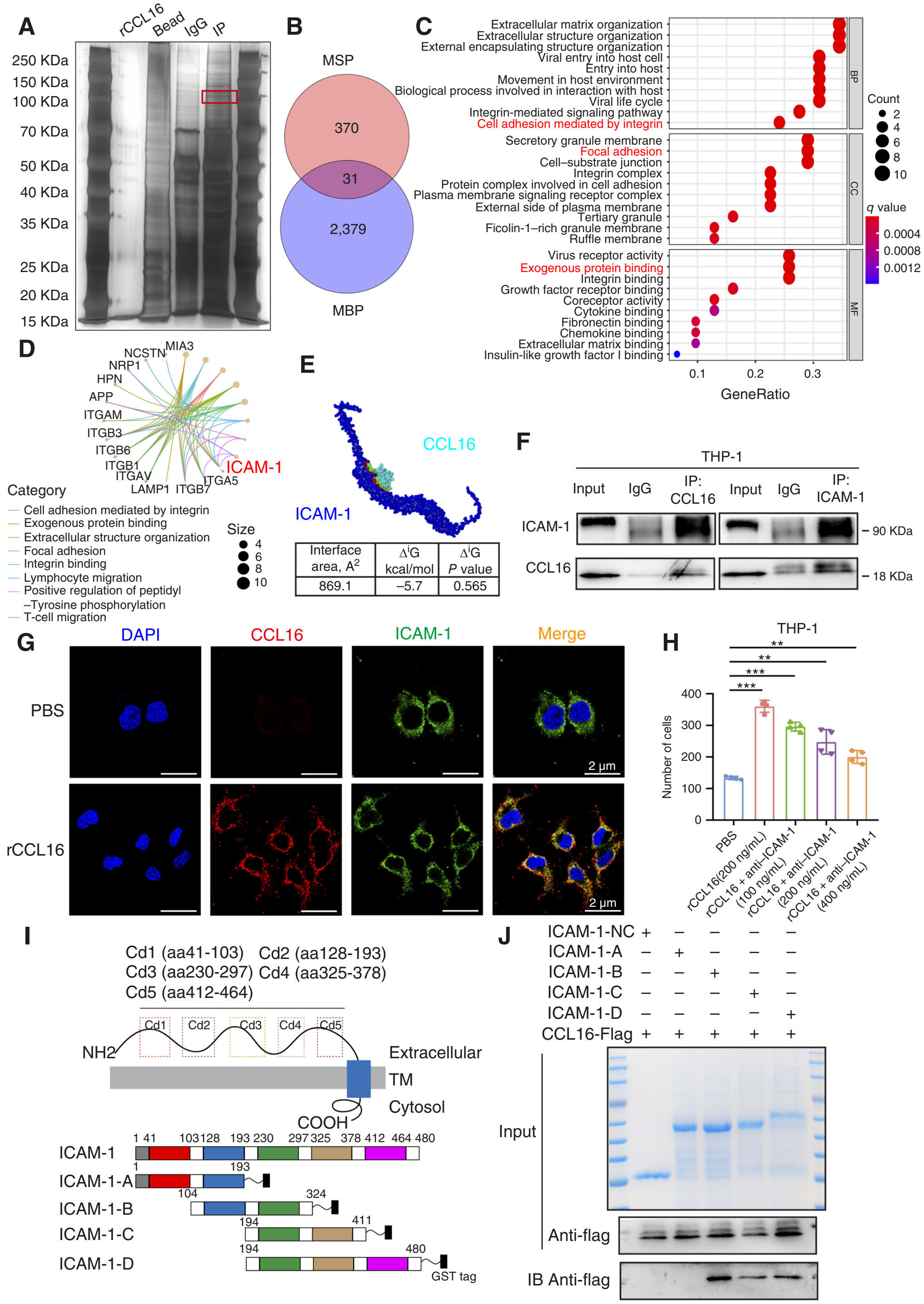

Figure 4.

Exploring the specific interaction between CCL16 and ICAM-1 on macrophage membranes. **A,** Representative image of fast silver staining using rCCL16 and isolated igG in THP-1 cell–induced M0 macrophages with PMA (200 ng/mL). **B,** Thirty-one membrane proteins identified by mass spectrometry. MSP, mass spectrometry protein; MBP, membrance protein. **C** and **D,** Enrichment analysis results of 31 membrane proteins. **E,** Molecular docking analysis of the spatial binding between CCL16 and ICAM-1. **F,** Coimmunoprecipitation analysis of CCL16 with ICAM-1 in THP-1 cell–induced M0 macrophages. **G,** Representative IF co-staining of CCL16, ICAM-1, and DAPI in rCCL16-treated M0 macrophages. Scale bars, 2 μm. **H,** A quantitative graph showing the migrated number of M0 macrophages treated with rCCL16 (200 ng/mL), either alone or in combination with different concentrations of αICAM-1. **I,** Schematic diagram illustrating the construction of ICAM-1 control plasmid and four truncation mutants (ICAM-1-A, ICAM-1-B, ICAM-1-C, and ICAM-1-D) with a GST tag. **J,** Direct binding of CCL16-Flag to ICAM-1-Cd3 GST using GST pulldown assay. Statistical significance assessed using a one-way ANOVA (**H**). Representative of $n = 3$ independent experiments (**F, G,** and **J**). **, $P < 0.01$; ***, $P < 0.001$.

24 hours, followed by resting in fresh medium for an additional 24 hours. The M0 macrophages were then cocultured with recombinant CCL16 (rCCL16; 200 ng/mL) for 48 hours. After coculture, the cells were lysed using RIPA buffer, and equal amounts of protein were subjected to SDS-PAGE for separation. Protein bands were visualized by rapid silver staining. Specific protein bands

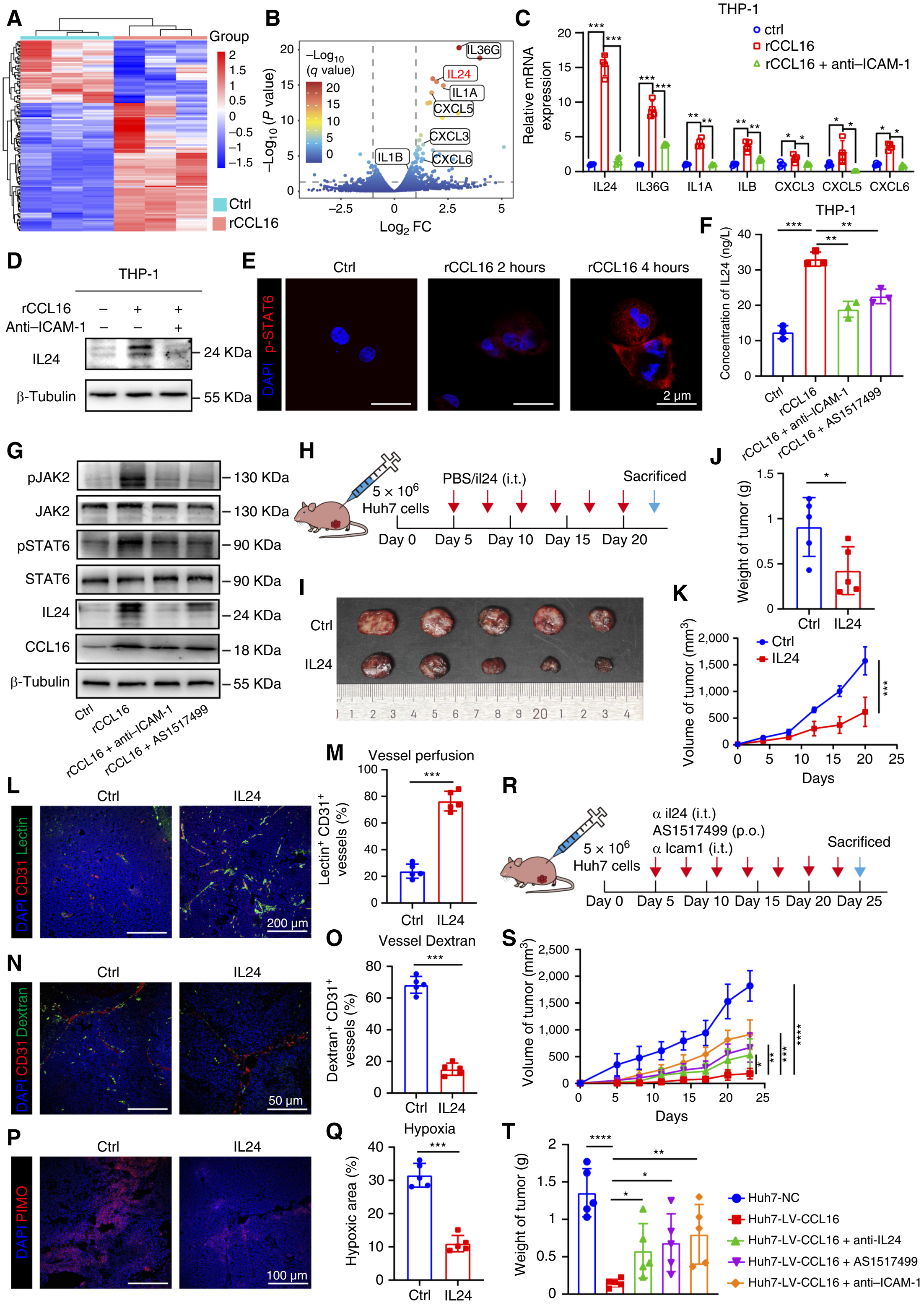

of interest were excised from the gel, digested with trypsin, and analyzed by mass spectrometry. The resulting peptide spectra were compared against membrane protein databases using Mascot software (RRID: SCR_014322) to identify membrane-associated proteins.

Coimmunoprecipitation assay

Coimmunoprecipitation was performed to examine the interaction between CCL16 and ICAM-1. M0 macrophages were stimulated with 200 ng/mL rCCL16 and cocultured for 48 hours. Briefly, cell lysates containing 500 μg of total protein were incubated with 2 μg of anti-CCL16 (YN1319, Immunoway) or anti–ICAM-1 (10831-1-AP, Proteintech) overnight at 4°C. The immune complexes were captured using Protein A/G agarose beads (Invitrogen) for 2 hours at 4°C. After incubation, the beads were washed three times with lysis buffer to remove nonspecifically bound proteins. The immunoprecipitates were eluted by boiling in SDS sample loading buffer for 5 minutes at 100°C. The samples were then subjected to SDS-PAGE and Western blot analysis to detect ICAM-1 in the CCL16 immunoprecipitate and CCL16 in the ICAM-1 immunoprecipitate. Detection was performed using corresponding primary antibodies, followed by HRP-conjugated secondary antibodies.

ELISA

ELISA kits for CCL16, VEGFA, and ANG2 were purchased from Cloud-Clone Corporation, whereas the IL24 ELISA kit was obtained from Guangzhou Tianyuan Biotechnology Corporation. All ELISA procedures were performed according to the manufacturer's instructions. Briefly, standards and samples were added to a 96-well plate pre-coated with specific antibodies and incubated. After washing to remove unbound components, biotin-conjugated detection antibodies were added and incubated. Following another wash, HRP-conjugated streptavidin was added for signal development. The optical density was measured at 450 nm using a microplate reader. Sample concentrations were calculated by comparison with a standard curve, and data were analyzed using GraphPad Prism 9.0 software.

Molecular docking

The Protein Data Bank (PDB) structures of CCL16 and ICAM-1 were retrieved from the PDB. Protein–protein docking was performed using GRAMM-X (http://gramm.compbio.ku.edu/), which employs Fast Fourier Transform algorithms for global interaction screening and binding conformation prediction. The resulting complexes were analyzed using PDBePISA (https://www.ebi.ac.uk/msd-srv/prot_int/) to evaluate interaction interfaces, including residue contacts, hydrophobic interactions, and hydrogen bonds.

Migration assay

Migration assays were performed using transwell chambers with 8-μm pore size inserts. THP-1 cells were differentiated into M0 macrophages by incubation with 100 nmol/L PMA for 24 hours, followed by a resting period of 24 hours. The M0 macrophages were seeded in the upper chamber, whereas rCCL16 (200 ng/mL) was added to the lower chamber. Different concentrations of ICAM-1 antibody were added to the upper chamber to antagonize the membrane receptors of THP-1 cells and observe the changes in macrophage migration. After 72 hours, the migrated macrophages in the lower chamber were fixed and stained.

Data availability

The RNA sequencing (RNA-seq) data from patients with HCC generated in this study are publicly available in the NCBI Sequence Read Archive database at BioProject PRJNA912860 (https://www.ncbi.nlm.nih.gov/search/all/?term=PRJNA912860). The macrophage transcriptomics data generated in this study are available in the NCBI Sequence Read Archive database at PRJNA1199572 (https://www.ncbi.nlm.nih.gov/bioproject/PRJNA1199572). The Cancer Genome Atlas-Liver HCC (TCGA-LIHC) RNA-seq data analyzed in this study were obtained from the Genomic Data Commons Data Portal (https://portal.gdc.cancer.gov/). The TCGA-LIHC dataset analyzed in this study was obtained through Tumor Immune Estimation Resource 1.0 (https://cistrome.shinyapps.io/timer/). CCL16 (ENSG00000275152) expression profiles across 54 tissues were obtained from Genotype-Tissue Expression (GTEx) V8 (Database of Genotypes and Phenotypes accession: phs000424.v8.p2; GTEx Portal: https://gtexportal.org). All other raw data generated in this study are available upon request from the corresponding author.

Results

Multiomics profiling identifies candidate hub molecules mediating vascular–immune cross-talk in HCC

Recent studies have identified CTCs in the bloodstream as an early marker of HCC metastasis (21, 25). Aberrant tumor vasculature and an immunosuppressive TME facilitate CTC invasion into the vasculature and their distant dissemination (2, 20). We utilized liquid biopsy technology to noninvasively quantify CTCs and

Figure 5.

CCL16–ICAM-1 interaction activates the JAK2/STAT6-IL24 axis in promoting vascular normalization. **A,** Transcriptome analysis of M0 macrophages treated with PBS or rCCL16 (200 ng/mL) for 2 days. **B,** Volcano plots showing the DEGs identified utilizing the Wilcoxon rank-sum test in M0 macrophages. **C,** mRNA levels of DEGs in THP-1 cell–induced M0 macrophages treated with rCCL16 (200 ng/mL), either alone or in combination with αICAM-1. **D,** Protein levels of IL24 in THP-1 cell–induced M0 macrophages treated with rCCL16 (200 ng/mL), either alone or in combination with αICAM-1. **E,** Representative IF images of M0 macrophages treated with rCCL16 (200 ng/mL) for 2 and 4 hours. Scale bars, 2 μm. **F,** ELISA analysis of IL24 in the culture supernatants of THP-1 cell–induced M0 macrophages treated with rCCL16 (200 ng/mL), either alone or in combination with αICAM-1 or AS1517499 for 2 days. **G,** Protein levels of pJAK2, JAK2, pSTAT6, STAT6, IL24, CCL16, and β-tubulin in THP-1 cell–induced M0 macrophages treated with rCCL16 (200 ng/mL), either alone or in combination with αICAM-1 or AS1517499. **H–K,** Scheme representing the experimental procedure (**H**), images of tumor size (**I**), tumor weight (**J**), and tumor growth curves (**K**) of nude mice injected subcutaneously with indicated cells with the treatment of PBS or ril24 (i.t., 5 μg per mouse, every 3 days). **L** and **M,** Representative IF images (**L**) and quantification (**M**) of vascular perfusion in indicated tumors using lectin fluorescence ($n = 5$). Scale bars, 200 μm. **N** and **O,** Representative IF images (**N**) and quantification (**O**) of vascular leakage in indicated tumors using dextran fluorescence ($n = 5$). Scale bars, 50 μm. **P** and **Q,** Representative IF images (**P**) and quantification (**Q**) of tissue hypoxia in indicated tumors using hypoxyprobe ($n = 5$). Scale bars, 100 μm. **R–T,** Scheme representing the experimental procedure (**R**), tumor growth curves (**S**), and tumor weight (**T**) of nude mice injected subcutaneously with indicated cells with treatment of αIL24 (i.t., 5 μg per mouse, every 3 days), AS1517499 (p.o., orally, 10 mg/kg, every 3 days), and αicam1 (i.t., 5 μg per mouse, every 3 days). Statistical significance assessed using one-way ANOVA (**C, F,** and **T**), two-tailed unpaired Student *t* test (**J, M, O,** and **Q**), and two-way ANOVA (**K** and **S**). Representative of $n = 3$ independent experiments (**D, E,** and **G**). *, $P < 0.05$; **, $P < 0.01$; ***, $P < 0.001$; ****, $P < 0.0001$.

revealed significant differences in the TME between HCC tissue samples with low CTC counts (CTC low, <3 CTCs) and those with high CTC counts (CTC high, ≥3 CTCs). We assessed CD31$^+$αSMA$^+$ vessels, which indicate pericyte coverage of endothelial cells, a key feature of vascular stabilization. Increased CD31$^+$αSMA$^+$ vessel density suggests improved vessel integrity and normalization of tumor vasculature (5, 26). Multiplex IHC demonstrated that the CTC-high group exhibited significantly reduced αSMA$^+$ pericyte

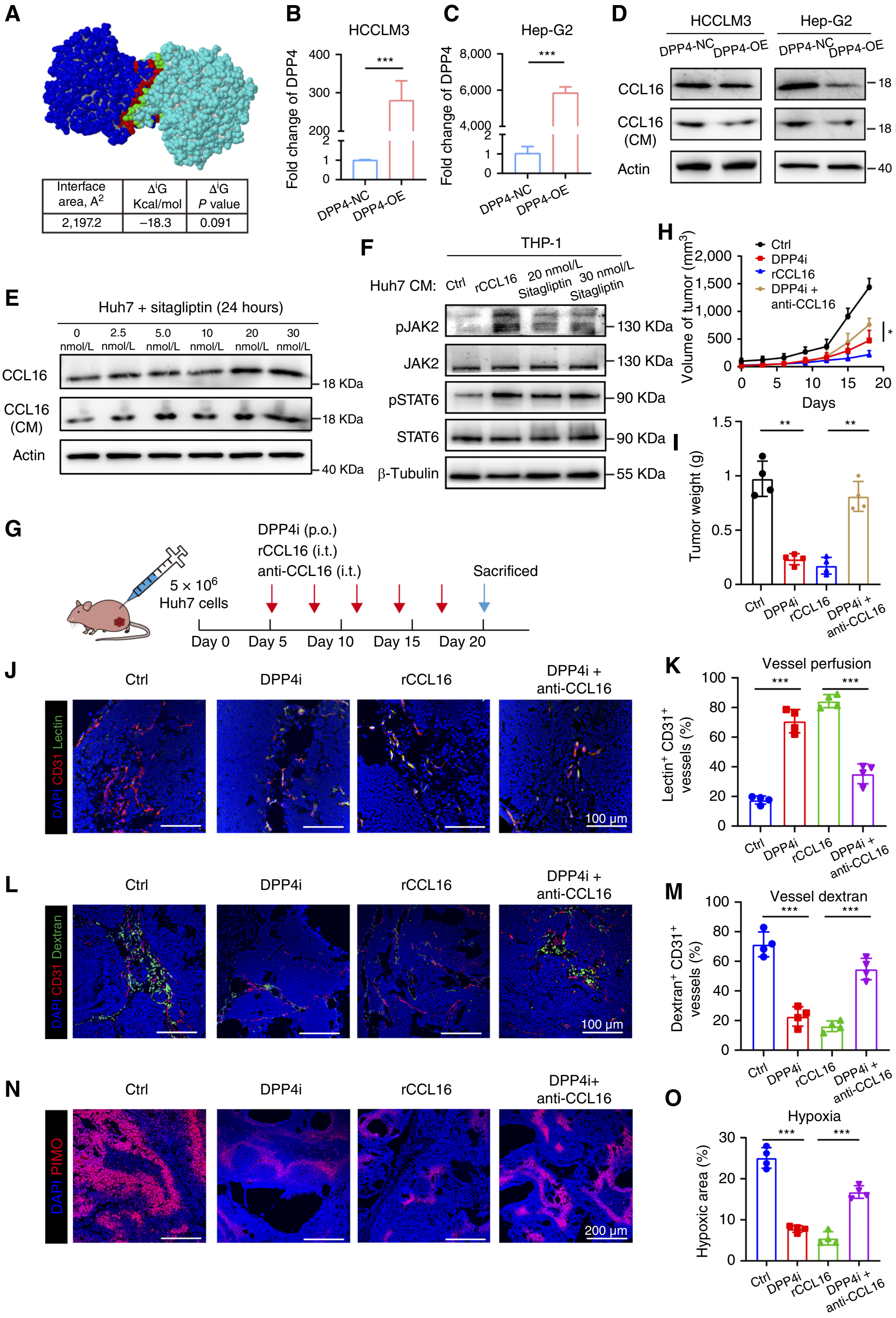

coverage of CD31$^+$ tumor vessels, along with markedly reduced infiltration of CD86$^+$ antitumor macrophages, CD8$^+$ T cells, and NK cells (**Fig. 1A** and **B**). These findings collectively indicate that HCC tissues with elevated CTC burdens are hallmarked by aberrant vascular architecture and an immunosuppressive TME, whose synergistic interplay constitutes a central driver of immune evasion in CTCs.

To elucidate the underlying mechanisms, we performed high-throughput sequencing on four CTC-low and four CTC-high HCC samples and integrated the results with data from the TCGA-LIHC dataset. We identified 294 DEGs (**Fig. 1C**; Supplementary Fig. S1A). Subsequently, through protein–protein interaction network analysis of the 294 DEGs using the cytoHubba tool, we identified CCL16 as one of the key genes in the core module (**Fig. 1D**). Notably, CCL16, specific expression in the liver, was the only gene significantly negatively correlated with the angiogenesis pathway in HCC tissues (Supplementary Fig. S1B and S1C). These findings implicate CCL16 as a potential regulator of vascular–immune cross-talk within the TME.

We generated CCL16-knockdown Hepa1-6 cell lines, with Hepa1-6-sh1 exhibiting the most significant knockdown efficiency (**Fig. 1E** and **F**). *In vivo* imaging results demonstrated that CCL16-knockdown Hepa1-6 cells significantly promoted tumor growth and metastasis in HCC (**Fig. 1G**). Cytometry by time-of-flight analysis revealed significant alterations in the tumor immune microenvironment (TIME) following CCL16 knockdown. The infiltration of effector immune cells, including DNT cells, pDCs, CD4 Tcm cells, and NK cells, was significantly reduced. Conversely, the proportion of immunosuppressive cell subsets, such as M2-like macrophages, myeloid-derived suppressor cells, CD103$^+$ dendritic cells, and regulatory T cells, significantly increased (**Fig. 1H** and **I**). Intriguingly, in CCL16-knockdown murine HCC models, the eosinophil subset exhibited substantial alterations, suggesting a critical role for CCL16 in shaping the inflammatory niche. Additionally, CCL16 knockdown significantly reduced αSMA$^+$ pericyte coverage on CD31$^+$ tumor vasculature, indicating disrupted vascular structural integrity (**Fig. 1J** and **K**). Collectively, these observations highlight CCL16 as a pivotal mediator orchestrating tumor vascular remodeling and TIME interactions in HCC.

CCL16 promotes vascular normalization and reverses immunosuppressive TME in HCC

Our study further elucidated the role of CCL16 in HCC. We first determined CCL16 expression levels in various HCC cell lines and measured secreted CCL16 in their supernatants (**Fig. 2A**). qPCR results confirmed that the Huh7 HCC cell line had relatively low CCL16 expression (**Fig. 2B**). To investigate the impact of CCL16 on tumor growth and the TIME, we constructed CCL16-overexpressing Huh7 cells (LV-CCL16) and corresponding control cells (LV-Ctrl). RT-qPCR and Western blot analyses confirmed significantly increased CCL16 protein and mRNA levels in the LV-CCL16 group (Supplementary Fig. S2A and S2B).

In vivo experiments, using a subcutaneous tumor model in nude mice, demonstrated that tumors in the LV-CCL16 group grew significantly slower compared with those in the LV-Ctrl group (**Fig. 2C**; Supplementary Fig. S2C), with reduced tumor weight (**Fig. 2D**). Tumor growth inhibition was concomitant with enhanced vascular normalization in the LV-CCL16 group, as demonstrated by elevated αSMA$^+$ pericyte coverage (**Fig. 2E** and **F**) and a significantly increased proportion of lectin$^+$CD31$^+$ functional vessels exhibiting improved perfusion efficiency (**Fig. 2G** and **H**). These findings suggest that CCL16 promotes more stable and functional tumor vasculature. Furthermore, IHC staining revealed that, compared with the control group displaying tortuous and irregular tumor vasculature characterized by abnormal dilation, structural disorganization, and diminished pericyte coverage, the LV-CCL16 group exhibited well-organized vascular morphology with neovascularization-like patterning and significantly elevated pericyte coverage (Supplementary Fig. S2D). Moreover, F4/80$^+$ macrophage infiltration was significantly increased in the LV-CCL16 group (**Fig. 2I** and **J**). In the C57 mouse orthotopic liver cancer model, tissue fluorescence analysis revealed reduced vascular perfusion (**Fig. 2K**; Supplementary Fig. S2E), enhanced vascular leakage (**Fig. 2L**; Supplementary Fig. S2F), and increased hypoxia (**Fig. 2M**; Supplementary Fig. S2G) in the Hepa1-6-sh group. These characteristics are important hallmarks of impaired TVN (12). Our study indicates that targeting CCL16 may be a promising strategy for normalizing tumor vasculature and modulating the TIME, potentially improving therapeutic outcomes for patients with HCC.

Building on the vascular–immune cross-talk defects observed in CCL16-knockdown models, we further investigated the therapeutic potential of exogenous rCCL16 in modulating tumor vasculature and the TIME. Subcutaneous tumor models were established in immunocompetent C57BL/6 mice (Supplementary Fig. S3A). rCCL16 administration markedly suppressed HCC progression, as evidenced by significantly reduced tumor growth and tumor weights compared with controls (**Fig. 2N** and **O**; Supplementary Fig. S3B). Vascular perfusion assays demonstrated enhanced tumor vascular perfusion efficiency in the rCCL16-treated group (**Fig. 2P**; Supplementary Fig. S3C). IHC analysis corroborated the enhanced CD8$^+$ T-cell infiltration in rCCL16-treated tumors (Supplementary Fig. S3D). Flow cytometric analysis of tumor tissues revealed a significant increase in T-cell infiltration (**Fig. 2Q**). Although the

Figure 6.

CCL16 degradation in the HCC microenvironment and therapeutic potential of DPP4i. **A,** Molecular docking analysis of the spatial binding between CCL16 and DPP4. **B** and **C,** mRNA levels of DPP4 in HCCLM3 cells (**B**) and Hep-G2 cells (**C**) with DPP4 overexpression. **D,** Protein levels of CCL16, CCL16 (CM, conditioned medium), and actin in HCCLM3 cells and Hep-G2 cells after DPP4 overexpression. **E,** Protein levels and secreted protein in conditioned media of CCL16 in Huh7 cell treated with sitagliptin for 24 hours in different concentrations. **F,** Protein levels of pJAK2, JAK2, pSTAT6, STAT6, and β-tubulin in THP-1 cell–induced M0 macrophages stimulated by conditioned media of Huh7 cells after treatment with rCCL16 (200 ng/mL), 20 nmol/L sitagliptin, and 30 nmol/L sitagliptin for 6 hours. **G–I,** Scheme representing the experimental procedure (**G**), tumor growth curves (**H**), and tumor weight (**I**) of nude mice injected subcutaneously with indicated cells with the treatment of DPP4i (orally, 10 mg/kg, every 3 days), rCCL16 (i.t., 2 μg per mouse, every 3 days), and DPP4i in combination with αCCL16 (i.t., 5 μg per mouse, every 3 days). **J** and **K,** Representative IF images (**J**) and quantification (**K**) of vascular perfusion in indicated tumors using lectin fluorescence ($n = 4$). Scale bars, 100 μm. **L** and **M,** Representative IF images (**L**) and quantification (**M**) of vascular leakage in indicated tumors using dextran fluorescence ($n = 4$). Scale bars, 100 μm. **N** and **O,** Representative IF images (**N**) and quantification (**O**) of tissue hypoxia in indicated tumors using hypoxyprobe ($n = 4$). Scale bars, 200 μm. Statistical significance assessed using two-tailed unpaired Student *t* test (**B** and **C**), two-way ANOVA (**H**), and one-way ANOVA (**I, K, M,** and **O**). Representative of $n = 3$ independent experiments (**D, E,** and **F**). *, $P < 0.05$; **, $P < 0.01$; ***, $P < 0.001$.

proportion of CD4$^+$ T cells remained unchanged, rCCL16 treatment substantially expanded CD8$^+$ T-cell infiltration and the CD8$^+$ cytotoxic T-cell subset, with elevated infiltration of effector immune cells including IFNγ$^+$CD8$^+$ T cells and GZMB$^+$CD8$^+$T cells, alongside reduced FOXP3$^+$CD4$^+$ regulatory T cells (**Fig. 2R**; Supplementary Fig. S3E). These findings collectively demonstrate that

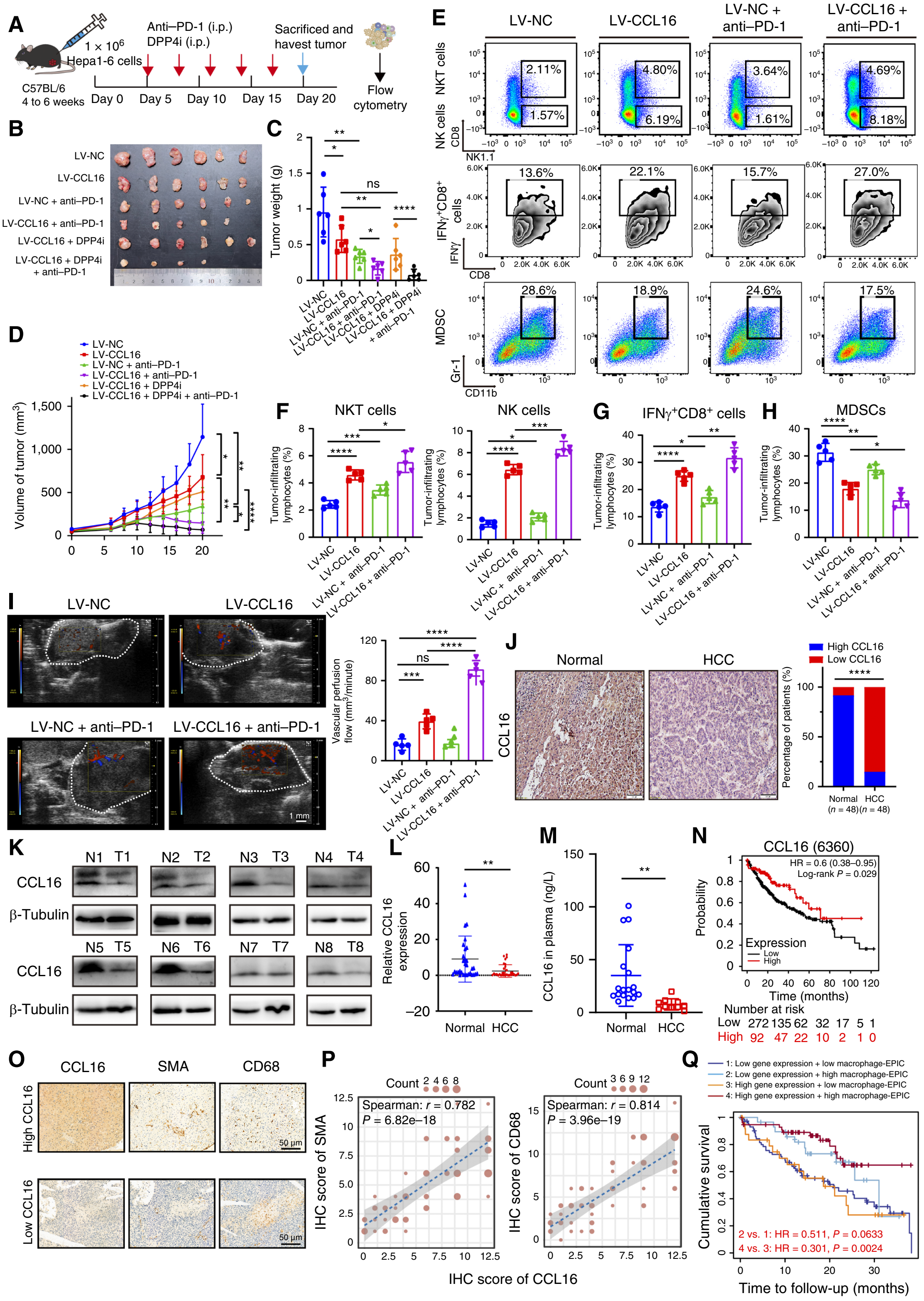

exogenous CCL16 exerts potent antitumor effects through dual mechanisms—synergistically promoting TVN and immune activation. This dual mechanism of action provides a novel rationale for developing vascular–immune coregulation therapeutic strategies in HCC.

CCL16 regulates macrophage-mediated TVN

Macrophages play an important role in regulating tumor vascular, and our study supposes the role of macrophages in CCL16-regulated TVN (**Fig. 2I** and **J**). Although prior work established CCL16's proangiogenic activity via CCR1 receptor signaling (27), LV-CCL16–overexpressing nude mouse model supplemented with the CCR1 antagonist ZK811752 (28) demonstrated preserved tumor vascular perfusion despite receptor blockade. Notably, this effect was independent of CCR1 (**Fig. 3A–C**; Supplementary Fig. S4A).

TIMER immune infiltration analysis identified a robust correlation between CCL16 expression and macrophage infiltration (**Fig. 3D**). Although LV-CCL16 + PBS treatment significantly inhibited tumor growth (**Fig. 3E** and **F**) and weight (**Fig. 3G**), these effects were reversed upon clodronate liposomes (29, 30) administration (Supplementary Fig. S4B), accompanied by reduced F4/80$^+$ macrophage-to-tumor cell ratios (**Fig. 3H** and **I**). Functional assessments demonstrated that LV-CCL16 + PBS enhanced vascular perfusion (**Fig. 3J** and **K**), reduced vascular leakage (**Fig. 3L** and **M**), and improved tissue oxygenation (**Fig. 3N** and **O**), whereas these benefits were abolished by macrophage depletion. Notably, PMA-induced M0 macrophages exhibited minimal endogenous CCL16 expression compared with hepatocytes and HCC cell lines (Supplementary Fig. S4C), supporting a paracrine mechanism of action. Stimulation of PMA-induced M0 macrophages with rCCL16 at varying concentrations suggested that 200 and 400 ng/mL significantly enhanced macrophage migration (Supplementary Fig. S4D).

These findings establish macrophages as indispensable mediators of CCL16-driven vascular normalization. The cytokine's ability to enhance perfusion, stabilize vasculature, and alleviate hypoxia is macrophage dependent, as evidenced by functional reversal upon macrophage ablation. Our work unveils a macrophage-centric paradigm for CCL16-mediated vascular remodeling, offering novel therapeutic strategies to potentiate antitumor immunity in HCC through macrophage modulation.

Exploring the specific interaction between CCL16 and ICAM-1 on macrophage membranes

To delineate the mechanism of CCL16–receptor binding on macrophages, we performed systematic experiments. PMA-differentiated M0 macrophages derived from THP-1 monocytes were cocultured with rCCL16 for 48 hours. Immunoprecipitation (IP) followed by electrophoresis with rapid silver staining revealed a distinct 70 to 100 kDa band in IP group, which was absent in IgG controls (**Fig. 4A**). Integrated mass spectrometry and membrane protein database screening identified 31 overlapping candidates, with ICAM-1 ranking among top hits (**Fig. 4B**; Supplementary Fig. S5A). Kyoto Encyclopedia of Genes and Genomes enrichment analysis highlighted these overlapping proteins' involvement in cell adhesion, migration, and related pathways (**Fig. 4C** and **D**).

IHC and immunofluorescence (IF) analyses of tissues from patients with HCC revealed predominant ICAM-1 expression in stromal cells, with TAMs exhibiting significantly higher ICAM-1 levels compared with T cells (Supplementary Fig. S5B and S5C). Molecular docking predicted spatial CCL16–ICAM-1 interaction with a binding affinity of −5.7 kcal/mol (**Fig. 4E**), later confirmed by reciprocal IP assays (**Fig. 4F**).

Cellular IF demonstrated exogenous rCCL16 colocalization with ICAM-1 on THP-1–derived M0 macrophages, absent in untreated controls (**Fig. 4G**). *In vitro* migration assays showed rCCL16-induced macrophage chemotaxis, which was dose-dependently attenuated by ICAM-1 antibody blockade (**Fig. 4H**; Supplementary Fig. S5D). To delineate the CCL16-binding domain of ICAM-1, we generated a GST-tagged ICAM-1 control plasmid alongside four truncation constructs (ICAM1-A/B/C/D; **Fig. 4I**). GST-tagged ICAM-1 truncations were expressed and purified from a prokaryotic system, while CCL16-Flag was expressed in HEK293T cells. GST pull-down assays demonstrated that Flag-CCL16 antibodies specifically coprecipitated ICAM1-B, ICAM1-C, and ICAM1-D, mapping the interaction to the Cd3 domain (amino acids 230-297) of ICAM-1 (**Fig. 4J**). These results establish the Cd3 region as the critical interface for CCL16-mediated macrophage functional modulation.

These findings suggest that the specific interaction between CCL16 and ICAM-1 on the macrophage membrane may play a crucial role in regulating macrophage activity, subsequently influencing TVN and the TIME. This understanding provides a potential new therapeutic target for modulating macrophages to regulate the TIME.

CCL16 promotes macrophage activation and TVN via ICAM-1–mediated molecular mechanisms

Our findings establish CCL16 as a critical regulator of immune activation and vascular normalization within the TME. Although ICAM-1 was identified as the key receptor in macrophage mediating these effects, its downstream signaling mechanisms remained undefined. To address this, we investigated how the CCL16–ICAM-1 interaction drives macrophage functional reprogramming.

Figure 7.

Clinical significance of CCL16 in HCC and exploration of combined treatment strategies. **A–D,** Scheme representing the experimental procedure (**A**), images of tumor size (**B**), tumor weight (**C**), and tumor growth curves (**D**) of C57BL/6 injected subcutaneously with indicated cells with the treatment of αPD-1 and DPP4i either alone or in combination with them. **E–H,** Flow cytometric analysis showing NKT cells, NK cells, IFNγ$^+$CD8$^+$T cells, and myeloid-derived suppressor cells (MDSC) in indicated tumors (**E**), with quantitation of different immune cells (**F–H**). $n = 5$ mice each. **I,** Representative images and quantification of tumor vascular perfusion within indicated tumors with or without αPD-1 treatment using Doppler ultrasound. **J,** Representative IHC images and percentage of high and low expression of CCL16 in 48 normal patients and 48 patients with HCC. **K,** Protein levels of CCL16 in eight human HCC tissues and matched adjacent normal tissues. **L,** mRNA levels of CCL16 in 32 normal patients and 32 patients with HCC. **M,** The concentration of serum CCL16 in 18 healthy volunteers (normal) and 10 patients with HCC (HCC). **N,** Kaplan–Meier survival curves for patients with HCC with distinct expression levels of CCL16 based on the liver cancer RNA-seq in Kaplan–Meier plotter. **O** and **P,** Representative IHC images (**O**) and the correlation between CCL16 and SMA$^+$ vessels in 81 patients or CCL16 and CD68$^+$ macrophages in 76 patients (**P**). **Q,** The cumulative survival curves for patients with HCC with distinct expression levels of CCL16 and distinct infiltration levels of macrophages using TIMER. Statistical significance assessed using two-way ANOVA (**D**), one-way ANOVA(**C** and **F–I**), two-tailed unpaired Student *t* test (**L** and **M**), χ^2 test (**J**), log-rank test (**N** and **Q**), and two-tailed Pearson correlation coefficient (**P**). Representative of $n = 3$ independent experiments (**K**). ns, not significant; *, $P < 0.05$; **, $P < 0.01$; ***, $P < 0.001$; ****, $P < 0.0001$.

Comprehensive evaluation of canonical angiogenesis regulators (Tie2, VEGFA, and Ang2) in rCCL16-stimulated M0 macrophages showed no significant changes via qPCR (Supplementary Fig. S6A), Western blotting (Supplementary Fig. S6B), or ELISA (Supplementary Fig. S6C and S6D), excluding their involvement in CCL16-mediated vascular normalization. Extended screening of 15 additional vascular mediators, including PDGFB, PLGF, CSF1, MRC1, MMP9, HGF, IL6, IL8, BV8, CXCL9, DLL4, PIGF, HIF1α, and IL10, revealed minimal mRNA alterations, except for significant PIGF and HIF1α downregulation and mild IL10 upregulation (Supplementary Fig. S6E). These results highlight CCL16's unique functionality, alleviating hypoxia while modestly amplifying immunosuppression via noncanonical pathways.

RNA-seq of rCCL16-stimulated M0 macrophages (**Fig. 5A**) uncovered pronounced upregulation of secretory factors, including IL24, IL36G, IL1A, IL1B, CXCL3, CXCL5, and CXCL6, with IL24 showing the highest induction (**Fig. 5B** and **C**). In THP-1 cells, rCCL16-driven IL24 expression was abolished by ICAM-1 blockade (**Fig. 5D**), confirming receptor dependency. Gene set enrichment analysis linked CCL16/ICAM-1 signaling to JAK–STAT activation (Supplementary Fig. S7A and S7B). Previous studies have demonstrated that STAT6 signaling is required for IL24 expression (31–33). IF and Western blotting demonstrated rCCL16-induced phosphorylation of STAT6 in a time-dependent manner (**Fig. 5E**), with concomitant upregulation of pJAK2, pSTAT6, and IL24 protein levels. These effects were reversed by ICAM-1 antibodies or the STAT6 inhibitor AS1517499 (34), corroborated by ELISA (**Fig. 5F** and **G**). Subcutaneous HCC models treated with recombinant IL24 (**Fig. 5H**) exhibited suppressed tumor growth (**Fig. 5I–K**), improved vascular perfusion (**Fig. 5L** and **M**), reduced vascular leakage (**Fig. 5N** and **O**), and attenuated hypoxia (**Fig. 5P** and **Q**). Conversely, neutralizing IL24 antibodies, AS1517499, or ICAM-1 blockade reversed the antitumor effects of CCL16 overexpression (**Fig. 5R–T**; Supplementary Fig. S7C).

These results delineate a CCL16–ICAM-1–JAK2/STAT6–IL24 axis as the mechanistic cornerstone of macrophage-driven TVN and tumor suppression. This pathway offers novel therapeutic targets for HCC immunotherapy by simultaneously modulating vascular integrity and immune activity within the TME.

CCL16 degradation in the HCC microenvironment and therapeutic potential of DPP4i

To investigate the mechanism of CCL16 downregulation in HCC, we explored whether oncogenic drivers promote CCL16 degradation. Based on prior evidence that administration of the DPP4i sitagliptin resulted in elevated concentrations of the chemokine CCL11 (35, 36), we hypothesized that DPP4, overexpressed in HCC, mediates CCL16 proteolysis.

Molecular docking predicted spatial interaction between DPP4 and CCL16 with a binding affinity of −18.3 kcal/mol (**Fig. 6A**). Overexpression of DPP4 in HCCLM3 and HepG2 cells (**Fig. 6B** and **C**) significantly reduced intracellular and secreted CCL16 levels (**Fig. 6D**), confirming its degradative role. *In vitro* validation showed that coincubation of recombinant DPP4 and rCCL16 led to time-dependent CCL16 degradation, reversible by sitagliptin (Supplementary Fig. S8A). Treating Huh7 cells with sitagliptin concentration dependently restored CCL16 levels in both lysates and supernatants (**Fig. 6E**), demonstrating DPP4i's capacity to stabilize CCL16. Functional consequences were assessed using conditioned medium from sitagliptin-treated Huh7 cells. Conditioned medium–stimulated M0 macrophages upregulated pJAK2 and pSTAT6 (**Fig. 6F**), reactivating the CCL16–ICAM-1–JAK2/STAT6 pathway.

In vivo, DPP4i (sitagliptin) or rCCL16 administration in subcutaneous HCC models (**Fig. 6G**) similarly suppressed tumor growth and weight, whereas anti-CCL16 + DPP4i cotreatment reversed this effect (**Fig. 6H** and **I**; Supplementary Fig. S8B), confirming DPP4i's reliance on CCL16 for therapeutic efficacy. Functional vascular analysis demonstrated that DPP4i treatment significantly improved perfusion efficiency (**Fig. 6J** and **K**), reduced vascular leakage (**Fig. 6L** and **M**), and alleviated hypoxia (**Fig. 6N** and **O**). These effects were comparable with rCCL16-mediated vascular normalization but were largely abolished upon CCL16 blockade.

These findings delineate DPP4-driven CCL16 degradation as a key immunosuppressive mechanism in HCC and position DPP4i as promising agents to amplify CCL16-mediated vascular–immune remodeling in the TME.

Clinical significance of CCL16 in HCC and exploration of combined therapeutic strategies

Although vascular normalization alone may be insufficient for optimal antitumor efficacy in advanced HCC, we evaluated its synergy with anti–PD-1 immunotherapy. Lentivirus-mediated CCL16-overexpressing cell lines (Supplementary Fig. S9A) were used in immunocompetent C57BL/6 mice under various treatment regimens (**Fig. 7A**). LV-CCL16–induced vascular normalization moderately enhanced antitumor activity comparable with anti–PD-1 monotherapy. Strikingly, combining LV-CCL16 with anti–PD-1 antibody achieved superior tumor suppression. Although combining LV-CCL16 with DPP4i (sitagliptin) amplified antitumor effects, no significant additive benefit over LV-CCL16 alone was observed, suggesting vascular normalization alone may not fully unlock therapeutic potential. However, sitagliptin-stabilized CCL16 expression synergized with anti–PD-1 to maximize efficacy (**Fig. 7B–D**).

Flow cytometry (**Fig. 7E**) revealed that anti–PD-1 monotherapy modestly improved the TIME, whereas LV-CCL16 significantly increased infiltration of NKT cells, NK cells (**Fig. 7F**), and IFNγ$^+$-CD8$^+$ T cells (**Fig. 7G**), while reducing myeloid-derived suppressor cells (**Fig. 7H**). CD8$^+$ T-cell proportions increased in LV-CCL16 and combination groups, with no change in CD4$^+$ T cells after vascular normalization (Supplementary Fig. S9B). The LV-CCL16 + anti–PD-1 group exhibited the most robust TIME improvement. Doppler ultrasound confirmed that LV-CCL16 enhanced vascular perfusion within the tumor without altering total vascular density (Supplementary Fig. S9C), with maximal perfusion achieved in the combination group (**Fig. 7I**). This aligns with reports that PD-1 blockade synergizes with vascular-targeting strategies to enhance drug delivery and antitumor efficacy (37–39), establishing a positive feedback loop between TVN and perfusion.

To assess the clinical significance of CCL16 in HCC, we performed IHC staining on 48 paired normal liver and HCC tissues. The results demonstrated a marked reduction in CCL16 expression in tumor tissues compared with adjacent normal liver tissues (**Fig. 7J**). Western blot analysis of eight paired samples further confirmed significantly diminished CCL16 protein levels in HCC tissues (**Fig. 7K**). mRNA analysis of 32 HCC and 32 normal liver tissues revealed pronounced downregulation of CCL16 mRNA in tumors (**Fig. 7L**). Given CCL16's secretory nature, we quantified

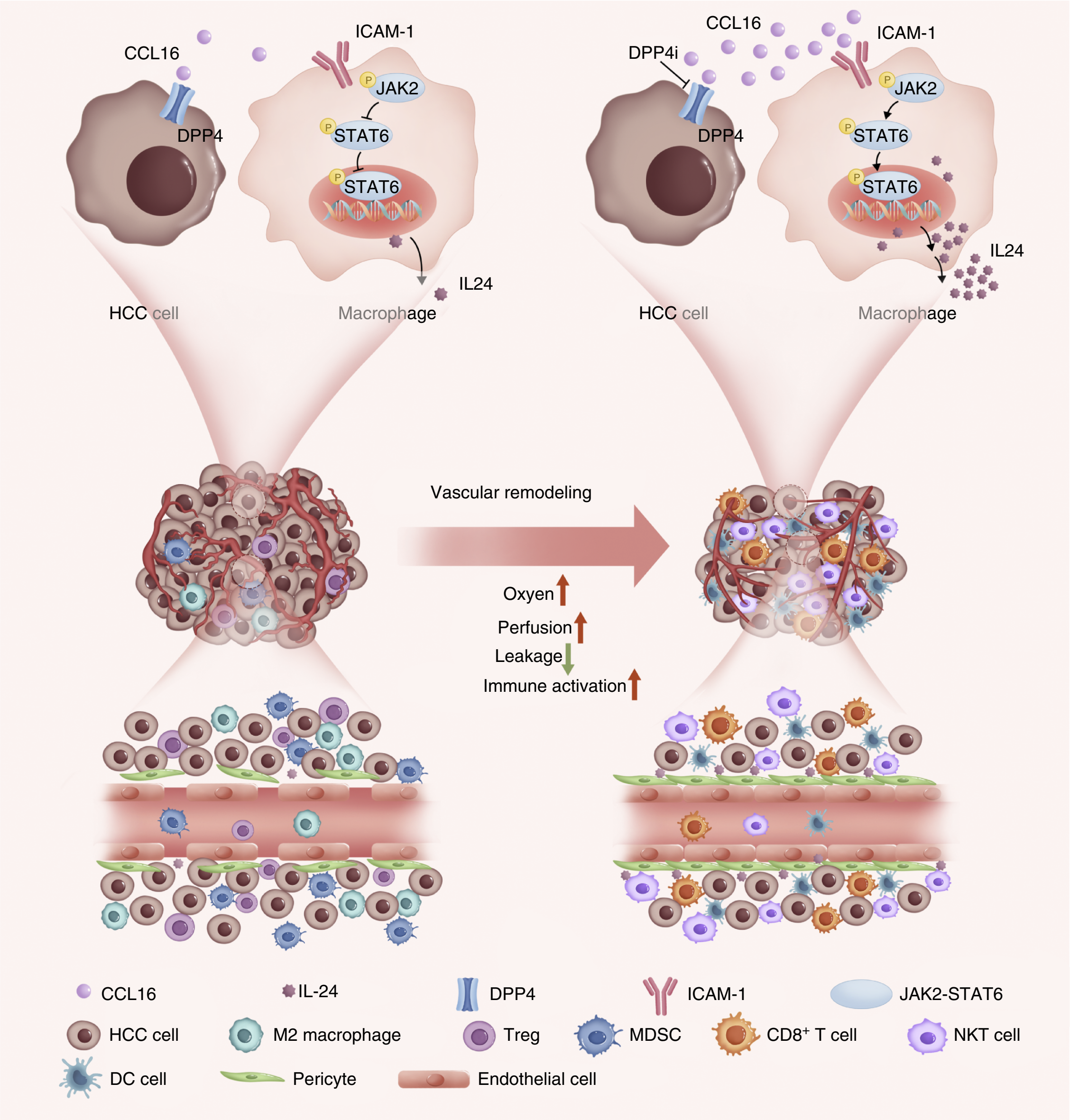

Figure 8.

Schematic illustration of tumor-derived CCL16 normalizing tumor vasculature through macrophage ICAM-1 receptor and enhancing immunotherapy efficacy in HCC. Top, schematic of the interaction between HCC cells and TAMs illustrating that CCL16, increased by DPP4 inhibitors in the TME, acts on ICAM-1 receptors on TAMs, activating the JAK2–STAT6 pathway and promoting IL24 expression and secretion. Middle, a macroscopic illustration of HCC depicting tumor vascular remodeling toward normalization and alterations in the immune microenvironment. Bottom, the microscopic schematic of tumor vasculature illustrating how vascular normalization, enhanced by CCL16, improves the TIME and strengthens antitumor effects. DC, dendritic cell; MDSC, myeloid-derived suppressor cell; Treg, regulatory T cell. Created with Adobe Photoshop CC 2020 by KL. Chen.

circulating CCL16 levels via ELISA in peripheral blood from 10 patients with HCC and 18 healthy controls, observing significantly lower serum CCL16 concentrations in patients with HCC (**Fig. 7M**). Kaplan–Meier survival analysis of patients with HCC revealed that high CCL16 expression correlated with improved overall survival (**Fig. 7N**). IHC assay in 81 normal and 76 HCC tissues identified significant positive associations between CCL16 expression and pericyte coverage (αSMA) and macrophage infiltration (CD68; **Fig. 7O** and **P**). Complementary analysis using the TIMER database demonstrated that patients with HCC with high CCL16 expression and concurrent macrophage enrichment exhibited the longest survival, whereas those with low CCL16 and reduced macrophage infiltration had the poorest outcomes (**Fig. 7Q**).

In conclusion, the synergistic combination of CCL16-driven TVN and PD-1 blockade represents a transformative strategy to enhance immunotherapy efficacy in HCC, addressing the clinical challenge of treatment resistance in advanced HCC.

Discussion

Multiple CC-family chemokines regulate immune cell recruitment with divergent pro/antitumor effects (40, 41). Although CCL16 is known to attract lymphocytes, monocytes, and dendritic cells (42, 43), its role in HCC, particularly in vascular–immune cross-talk, remained undefined. Our multiomics screening identified CCL16 as a hub molecule governing vascular normalization and immune remodeling in HCC and involved in the progression and metastasis of CTCs. CCL16 overexpression rectified vascular abnormalities and alleviated immunosuppression, whereas its deficiency exacerbated these phenotypes.

CCL16 exhibits context-dependent functional complexity. Although *in vitro* studies suggest proangiogenic roles in non-HCC models (27), its vascular regulatory effects in HCC, characterized by aberrant vasculature and immunosuppression, require validation in *in vivo* and clinical contexts. Clinical data reveal marked CCL16 downregulation in HCC tissues and patient serum compared with normal counterparts. Intriguingly, CCL16 overexpression induced vascular normalization as evidenced by increased pericyte coverage and improved perfusion efficiency, leading to reduced vascular leakage and hypoxia, without accelerating tumor growth, reconciling its paradoxical roles across cancers. CCL16 stabilizes vasculature through structural remodeling rather than pathologic angiogenesis. The synergy between CCL16-induced normalization and anti–PD-1 therapy underscores its therapeutic immunomodulation potential. However, there are still some aspects that require further exploration. Although the tumor growth inhibition observed with CCL16 overexpression seems counterintuitive given the absence of direct drug delivery or effector immune cell engagement, our findings suggest multiple mechanisms may underlie this phenomenon. (i) Vascular normalization alleviates hypoxia-driven proliferation and metastasis by improving oxygenation and reducing interstitial fluid pressure (4, 5, 8, 44); (ii) enhanced endothelial barriers restrict nutrient access like glutamine deprivation (45, 46) and mitigate Warburg effect–mediated lactate accumulation (47); (iii) antitumor macrophage reprogramming drives IL24 secretion, exerting antiangiogenic, stemness-suppressive, and proapoptotic effects (48–50); and (iv) CCL16 autonomously suppresses tumor growth via vascular stabilization independent of immune effector cells, analogous to chloroquine, which suppresses tumor growth and counteracts cancer cell invasion and metastasis by promoting vascular normalization independent of autophagy (51). In addition, to address the controversial pseudogene status of CCL16 (42, 52), we generated HCC murine models with lentiviral-mediated overexpression and knockdown of human CCL16, confirming its vascular–immune regulatory roles in HCC. Future work requires optimized biological tools and advanced models to fully delineate CCL16's spatiotemporal functions within the TIME. These efforts will accelerate therapeutic development, leveraging CCL16's dual capacity to normalize vasculature and potentiate immunity.

The mechanistic model is illustrated in a schematic illustration (**Fig. 8**), which visually summarizes our proposed framework: tumor-derived CCL16, stabilized by DPP4 inhibition within the TME, binds to ICAM-1 receptors on TAMs, activates the JAK2–STAT6 signaling cascade, and induces IL24 secretion. These events collectively promote vascular normalization, enhance immune cell infiltration, and potentiate antitumor responses. The figure integrates macroscopic and microscopic depictions of CCL16-mediated vascular–immune remodeling in HCC, reinforcing its potential as a therapeutic axis in combination with immune checkpoint blockade.

Although chemokine–receptor interactions typically govern intercellular communication, our study uncovers a CCR1-independent vascular mechanism of CCL16 in HCC. Despite CCL16's known binding to CCR1 in hepatic cells (27) and facilitating eosinophil trafficking via a novel functional ligand H4 (53), we demonstrate that its TVN effects are mediated through macrophage ICAM-1, a high-affinity receptor identified via integrated approaches. This interaction drives macrophage recruitment and reprogramming, leading to IL24 secretion, a multifunctional IL10 family cytokine with antiangiogenic, immunostimulatory, and cancer stem cell–suppressive properties (50). Unlike transient VEGF-targeted approaches, CCL16 sustains vascular integrity without exacerbating hypoxia-driven metastasis by balancing pro/antiangiogenic factors, as evidenced by abolished normalization phenotypes upon macrophage depletion. Clinically, IL24's safety and efficacy in phase I/II clinical trials (54) and CCL16–IL24 signaling align with Jain TVN framework and address dosing challenges of conventional therapies. These findings establish ICAM-1–dependent macrophage reprogramming as a novel paradigm for vascular–immune cotargeting in HCC.

Emerging evidence implicates DPP4, an oncogene overexpressed in solid tumors, as a key regulator of chemokine stability via its extracellular dipeptidyl peptidase activity (55, 56). Our study elucidates that DPP4-mediated degradation drives the marked downregulation of CCL16 in the HCC microenvironment, a mechanism consistent with its known role in elevating CCL11 concentrations (35). Pharmacologic inhibition of DPP4 using sitagliptin, an FDA-approved antidiabetic agent (57), effectively stabilized CCL16, promoting sustained vascular normalization and antitumor immunity. Crucially, sitagliptin extends the therapeutic window of CCL16-induced vascular normalization, addressing the transient efficacy of conventional antiangiogenics. Although anti–PD-1 monotherapy shows limited efficacy in HCC (58) due to vascular-driven immunosuppression and drug delivery barriers (59, 60), the triple combination of DPP4 inhibition, CCL16 overexpression, and anti–PD-1 achieved synergistic tumor suppression. This strategy leverages DPP4i's repurposing potential and CCL16's dual role as a vascular stabilizer and immune adjuvant, with clinical relevance further supported by the correlation between CCL16 levels, macrophage infiltration, and patient survival, positioning CCL16 as a predictive biomarker for vascular–immune cotargeting therapies.

Authors' Disclosures

K. Chen reports grants from the National Natural Science Foundation of China and the Key Area Research and Development Program of Guangdong Province during the conduct of the study. J. Pei reports grants from the National Natural Science Foundation of China and the Key Area Research and Development Program of Guangdong Province during the conduct of the study. X. Wei reports grants from the National Natural Science Foundation of China and the Key Area Research and Development Program of Guangdong Province during the conduct of the study. M. Pan reports grants from the National Natural Science Foundation of China and the Key Area Research and Development Program of Guangdong Province during the conduct of the study. No disclosures were reported by the other authors.

Authors' Contributions

K. Chen: Data curation, formal analysis, supervision, validation, investigation, visualization, methodology, writing–original draft, project administration, writing–review and editing. **H. Feng:** Supervision, validation, investigation, visualization, methodology, writing–original draft. **Y. Zhang:** Validation, visualization, methodology, writing–original draft. **J. Pei:** Validation, investigation, methodology. **Y. Xu:** Validation, investigation. **X. Wei:** Validation, investigation. **Z. Chen:**

Validation, investigation. **Z. Feng:** Data curation, methodology. **L. Cai:** Formal analysis, supervision. **Y. Li:** Resources, supervision, funding acquisition. **L. Zhao:** Resources, data curation, supervision, funding acquisition. **M. Pan:** Resources, formal analysis, supervision, funding acquisition, investigation, writing–review and editing.

Acknowledgments

M. Pan was supported by the National Natural Science Foundation of China (grant/award number 82072627 and 82373159) and the Key Area Research and Development Program of Guangdong Province (grant/award number 2023B1111020008). This work was also supported by Science and Technology Projects in Guangzhou of China (grant/award number 2023B03J1247) and Clinical high-tech project in Guangzhou region (grant/award number 2024P-GX20). We sincerely acknowledge the TCGA, GEO database, and GSEA owners for providing their platforms and the contributors for uploading meaningful datasets. We employed DeepSeek AI and ChatGPT to improve the quality of the writing for specific sections of the manuscript. The authors affirm full responsibility for all scientific content, data analysis, and conclusions presented in this work.

Note

Supplementary data for this article are available at Cancer Research Online (http://cancerres.aacrjournals.org/).

Received November 13, 2024; revised March 31, 2025; accepted August 11, 2025; posted first August 12, 2025.

References

1. Fukumura D, Kloepper J, Amoozgar Z, Duda DG, Jain RK. Enhancing cancer immunotherapy using antiangiogenics: opportunities and challenges. Nat Rev Clin Oncol 2018;15:325–40.
2. Hilmi M, Neuzillet C, Calderaro J, Lafdil F, Pawlotsky JM, Rousseau B. Angiogenesis and immune checkpoint inhibitors as therapies for hepatocellular carcinoma: current knowledge and future research directions. J Immunother Cancer 2019;7:333.
3. Liu LP, Ho RL, Chen GG, Lai PB. Sorafenib inhibits hypoxia-inducible factor-1α synthesis: implications for antiangiogenic activity in hepatocellular carcinoma. Clin Cancer Res 2012;18:5662–71.
4. Jain RK. Normalization of tumor vasculature: an emerging concept in antiangiogenic therapy. Science 2005;307:58–62.
5. Goel S, Duda DG, Xu L, Munn LL, Boucher Y, Fukumura D, et al. Normalization of the vasculature for treatment of cancer and other diseases. Physiol Rev 2011;91:1071–121.
6. Huynh H, Lee LY, Goh KY, Ong R, Hao HX, Huang A, et al. Infigratinib mediates vascular normalization, impairs metastasis, and improves chemotherapy in hepatocellular carcinoma. Hepatology 2019;69:943–58.
7. Martin JD, Seano G, Jain RK. Normalizing function of tumor vessels: progress, opportunities, and challenges. Annu Rev Physiol 2019;81:505–34.
8. Viallard C, Larrivée B. Tumor angiogenesis and vascular normalization: alternative therapeutic targets. Angiogenesis 2017;20:409–26.
9. Ebos JM, Lee CR, Kerbel RS. Tumor and host-mediated pathways of resistance and disease progression in response to antiangiogenic therapy. Clin Cancer Res 2009;15:5020–5.
10. Huang M, Lin Y, Wang C, Deng L, Chen M, Assaraf YG, et al. New insights into antiangiogenic therapy resistance in cancer: mechanisms and therapeutic aspects. Drug Resist Updat 2022;64:100849.
11. Iwamoto H, Abe M, Yang Y, Cui D, Seki T, Nakamura M, et al. Cancer lipid metabolism confers antiangiogenic drug resistance. Cell Metab 2018;28:104–17.e5.
12. Park JS, Kim IK, Han S, Park I, Kim C, Bae J, et al. Normalization of tumor vessels by Tie2 activation and Ang2 inhibition enhances drug delivery and produces a favorable tumor microenvironment. Cancer Cell 2016;30:953–67.
13. Wang-Bishop L, Kimmel BR, Ngwa VM, Madden MZ, Baljon JJ, Florian DC, et al. STING-Activating nanoparticles normalize the vascular-immune interface to potentiate cancer immunotherapy. Sci Immunol 2023;8:eadd1153.
14. Huang Y, Kim BYS, Chan CK, Hahn SM, Weissman IL, Jiang W. Improving immune-vascular crosstalk for cancer immunotherapy. Nat Rev Immunol 2018;18:195–203.
15. Wenes M, Shang M, Di Matteo M, Goveia J, Martín-Pérez R, Serneels J, et al. Macrophage metabolism controls tumor blood vessel morphogenesis and metastasis. Cell Metab 2016;24:701–15.
16. Wang W, Li T, Cheng Y, Li F, Qi S, Mao M, et al. Identification of hypoxic macrophages in glioblastoma with therapeutic potential for vasculature normalization. Cancer Cell 2024;42:815–32.e12.
17. Rolny C, Mazzone M, Tugues S, Laoui D, Johansson I, Coulon C, et al. HRG inhibits tumor growth and metastasis by inducing macrophage polarization and vessel normalization through downregulation of PlGF. Cancer Cell 2011;19:31–44.
18. Chen X, Zhang L, Zhang IY, Liang J, Wang H, Ouyang M, et al. RAGE expression in tumor-associated macrophages promotes angiogenesis in glioma. Cancer Res 2014;74:7285–97.
19. Bruix J, da Fonseca LG, Reig M. Insights into the success and failure of systemic therapy for hepatocellular carcinoma. Nat Rev Gastroenterol Hepatol 2019;16:617–30.
20. Strilic B, Offermanns S. Intravascular survival and extravasation of tumor cells. Cancer Cell 2017;32:282–93.
21. Sun YF, Wu L, Liu SP, Jiang MM, Hu B, Zhou KQ, et al. Dissecting spatial heterogeneity and the immune-evasion mechanism of CTCs by single-cell RNA-Seq in hepatocellular carcinoma. Nat Commun 2021;12:4091.
22. Liu X, Song J, Zhang H, Liu X, Zuo F, Zhao Y, et al. Immune checkpoint HLA-E:CD94-NKG2A mediates evasion of circulating tumor cells from NK cell surveillance. Cancer Cell 2023;41:272–87.e9.
23. Nikanjam M, Kato S, Kurzrock R. Liquid biopsy: current technology and clinical applications. J Hematol Oncol 2022;15:131.
24. Ahn JC, Teng PC, Chen PJ, Posadas E, Tseng HR, Lu SC, et al. Detection of circulating tumor cells and their implications as a biomarker for diagnosis, prognostication, and therapeutic monitoring in hepatocellular carcinoma. Hepatology 2021;73:422–36.
25. Luo Q, Wang C, Peng B, Pu X, Cai L, Liao H, et al. Circulating tumor-cell-associated white blood cell clusters in peripheral blood indicate poor prognosis in patients with hepatocellular carcinoma. Front Oncol 2020;10:1758.
26. Xu Z, Guo C, Ye Q, Shi Y, Sun Y, Zhang J, et al. Endothelial deletion of SHP2 suppresses tumor angiogenesis and promotes vascular normalization. Nat Commun 2021;12:6310.
27. Strasly M, Doronzo G, Cappello P, Valdembri D, Arese M, Mitola S, et al. CCL16 activates an angiogenic program in vascular endothelial cells. Blood 2004;103:40–9.
28. Elices MJ. BX-471 berlex. Curr Opin Investig Drugs 2002;3:865–9.
29. Zeng X, Liu G, Peng W, He J, Cai C, Xiong W, et al. Combined deficiency of SLAMF8 and SLAMF9 prevents endotoxin-induced liver inflammation by downregulating TLR4 expression on macrophages. Cell Mol Immunol 2020;17:153–62.
30. Griesmann H, Drexel C, Milosevic N, Sipos B, Rosendahl J, Gress TM, et al. Pharmacological macrophage inhibition decreases metastasis formation in a genetic model of pancreatic cancer. Gut 2017;66:1278–85.
31. Chu KH, Chiang BL. CD200R activation on naïve T cells by B cells induces suppressive activity of T cells via IL-24. Cell Mol Life Sci 2024;81:231.
32. Sahoo A, Lee CG, Jash A, Son JS, Kim G, Kwon HK, et al. Stat6 and c-Jun mediate Th2 cell-specific IL-24 gene expression. J Immunol 2011;186:4098–109.
33. Dabitao D, Hedrich CM, Wang F, Vacharathit V, Bream JH. Cell-specific requirements for STAT proteins and type I IFN receptor signaling discretely regulate IL-24 and IL-10 expression in NK cells and macrophages. J Immunol 2018;200:2154–64.
34. Huang C, Wang J, Liu H, Huang R, Yan X, Song M, et al. Ketone body β-hydroxybutyrate ameliorates colitis by promoting M2 macrophage polarization through the STAT6-dependent signaling pathway. BMC Med 2022;20:148.
35. Hollande C, Boussier J, Ziai J, Nozawa T, Bondet V, Phung W, et al. Inhibition of the dipeptidyl peptidase DPP4 (CD26) reveals IL-33-dependent eosinophil-mediated control of tumor growth. Nat Immunol 2019;20:257–64.
36. Mulvihill EE, Drucker DJ. Pharmacology, physiology, and mechanisms of action of dipeptidyl peptidase-4 inhibitors. Endocr Rev 2014;35:992–1019.

37. Tokumasu M, Nishida M, Zhao W, Chao R, Imano N, Yamashita N, et al. Metformin synergizes with PD-1 blockade to promote normalization of tumor vessels via CD8T cells and IFNγ. Proc Natl Acad Sci U S A 2024;121:e2404778121.
38. Li Q, Wang Y, Jia W, Deng H, Li G, Deng W, et al. Low-dose anti-angiogenic therapy sensitizes breast cancer to PD-1 blockade. Clin Cancer Res 2020;26: 1712–24.
39. Ramjiawan RR, Griffioen AW, Duda DG. Anti-angiogenesis for cancer revisited: is there a role for combinations with immunotherapy?. Angiogenesis 2017;20:185–204.
40. Korbecki J, Kojder K, Simińska D, Bohatyrewicz R, Gutowska I, Chlubek D, et al. CC chemokines in a tumor: a review of pro-cancer and anti-cancer properties of the ligands of receptors CCR1, CCR2, CCR3, and CCR4. Int J Mol Sci 2020;21:8412.
41. Hao Q, Vadgama JV, Wang P. CCL2/CCR2 signaling in cancer pathogenesis. Cell Commun Signal 2020;18:82.
42. Guiducci C, Vicari AP, Sangaletti S, Trinchieri G, Colombo MP. Redirecting in vivo elicited tumor infiltrating macrophages and dendritic cells towards tumor rejection. Cancer Res 2005;65:3437–46.
43. Li J, Hu P, Khawli LA, Epstein AL. LEC/chTNT-3 fusion protein for the immunotherapy of experimental solid tumors. J Immunother 2003;26:320–31.
44. Vemuri K, de Alves Pereira B, Fuenzalida P, Subashi Y, Barbera S, van Hooren L, et al. CD93 maintains endothelial barrier function and limits metastatic dissemination. JCI Insight 2024;9:e169830.
45. Zhang Q, Wei T, Jin W, Yan L, Shi L, Zhu S, et al. Deficiency in SLC25A15, a hypoxia-responsive gene, promotes hepatocellular carcinoma by reprogramming glutamine metabolism. J Hepatol 2024;80:293–308.
46. Li Y, Li B, Xu Y, Qian L, Xu T, Meng G, et al. GOT2 silencing promotes reprogramming of glutamine metabolism and sensitizes hepatocellular carcinoma to glutaminase inhibitors. Cancer Res 2022;82:3223–35.
47. Yang Z, Yan C, Ma J, Peng P, Ren X, Cai S, et al. Lactylome analysis suggests lactylation-dependent mechanisms of metabolic adaptation in hepatocellular carcinoma. Nat Metab 2023;5:61–79.
48. Han D, Ma Q, Ballar P, Zhang C, Dai M, Luo X, et al. Reprogramming tumor-associated macrophages and inhibiting tumor neovascularization by targeting MANF-HSF1-HSP70-1 pathway: an effective treatment for hepatocellular carcinoma. Acta Pharm Sin B 2024;14:4396–412.
49. Wu Z, Liu W, Wang Z, Zeng B, Peng G, Niu H, et al. Mesenchymal stem cells derived from iPSCs expressing interleukin-24 inhibit the growth of melanoma in the tumor-bearing mouse model. Cancer Cell Int 2020;20:33.
50. Maes H, Kuchnio A, Peric A, Moens S, Nys K, De Bock K, et al. Tumor vessel normalization by chloroquine independent of autophagy. Cancer Cell 2014;26: 190–206.
51. Fukuda S, Hanano Y, Iio M, Miura R, Yoshie O, Nomiyama H. Genomic organization of the genes for human and mouse CC chemokine LEC. DNA Cell Biol 1999;18:275–83.
52. Nakayama T, Kato Y, Hieshima K, Nagakubo D, Kunori Y, Fujisawa T, et al. Liver-expressed chemokine/CC chemokine ligand 16 attracts eosinophils by interacting with histamine H4 receptor. J Immunol 2004;173:2078–83.
53. Whitaker EL, Filippov VA, Duerksen-Hughes PJ. Interleukin 24: mechanisms and therapeutic potential of an anti-cancer gene. Cytokine Growth Factor Rev 2012;23:323–31.
54. Emdad L, Bhoopathi P, Talukdar S, Pradhan AK, Sarkar D, Wang XY, et al. Recent insights into apoptosis and toxic autophagy: the roles of MDA-7/IL-24, a multidimensional anti-cancer therapeutic. Semin Cancer Biol 2020;66:140–54.
55. Enz N, Vliegen G, De Meester I, Jungraithmayr W. CD26/DPP4 - a potential biomarker and target for cancer therapy. Pharmacol Ther 2019;198: 135–59.
56. Nishina S, Yamauchi A, Kawaguchi T, Kaku K, Goto M, Sasaki K, et al. Dipeptidyl peptidase 4 inhibitors reduce hepatocellular carcinoma by activating lymphocyte chemotaxis in mice. Cell Mol Gastroenterol Hepatol 2019;7:115–34.
57. Deacon CF. Dipeptidyl peptidase 4 inhibitors in the treatment of type 2 diabetes mellitus. Nat Rev Endocrinol 2020;16:642–53.
58. Finn RS, Ryoo B-Y, Merle P, Kudo M, Bouattour M, Lim HY, et al. Pembrolizumab as second-line therapy in patients with advanced hepatocellular carcinoma in KEYNOTE-240: a randomized, double-blind, phase III trial. J Clin Oncol 2020;38:193–202.
59. Vesely MD, Zhang T, Chen L. Resistance mechanisms to anti-PD cancer immunotherapy. Annu Rev Immunol 2022;40:45–74.
60. Bao X, Shen N, Lou Y, Yu H, Wang Y, Liu L, et al. Enhanced anti-PD-1 therapy in hepatocellular carcinoma by tumor vascular disruption and normalization dependent on combretastatin A4 nanoparticles and DC101. Theranostics 2021;11: 5955–69.